Utrecht University

Utrecht University

Master of Science in Experimental Physics

Exploring the behavior of the strong coupling constant through the primary Lund plane for jets detected by the ALICE detector

---

Abstract

This thesis aims to explore the running of the strong coupling constant through the analysis of the Primary Lund plane for charged jets from proton-proton collisions at $\sqrt{s}$=13.6 TeV detected by the ALICE detector during the LHC Run 3 in 2022. First, the quality and reliability of the data used in this analysis have been ensured through a detailed track quality assurance. Subsequently, the first Primary Lund plane for Run 3 data has been constructed and the Primary Lund plane density has been analyzed with the aim of extracting information on the jet substructures and, specifically, on the running of the strong coupling constant. Moreover, the results are compared with other experimental measurements.

Author

Alice Caluisi

Supervisor

Dr. Marta Verweij

March 26, 2024

Contents

1 Introduction

Visible matter - from galaxies and stars to molecules and particles - is mostly made of hadrons, composite particles made of quarks bound together by the strong force. The strong force is the strongest among the four fundamental forces and it is described by Quantum Chromodynamics. The strong force has gluons as mediators, which "glue" quarks into hadrons, crafting the building blocks of the matter we experience every day. The strength of the strong force is quantified by the strong coupling constant α_s, which exhibits a unique running behavior across energy scales, explaining why the strong force is imperceptible in the macroscopic world, yet it reaches orders of magnitude hundreds of times larger than those of the other fundamental forces within the subatomic world. In fact, the strong coupling constant becomes large at short distances (or high energy scales), making the strong force strong. Conversely, it diminishes over larger distances (so low energy scales), reducing the strength of the strong force.

To unravel the complex dynamics of the strong force, this study focuses on analyzing jet production. Jets are collimated sprays of particles emanating from the fragmentation of high-energy quarks and gluons produced in high-energy particle collisions.

Specifically, this thesis delves into the exploration of the running of the strong coupling constant through a detailed analysis of the Primary Lund plane for charged jets emanating from proton-proton collisions at $\sqrt{s} =13.6$ TeV detected by the ALICE detector during the Run 3 of the LHC. The Primary Lund plane density serves as a tool to observe the running of the strong coupling constant and to extract information regarding the interactions within jet emissions.

An extensive theoretical overview of Quantum Chromodynamics and the strong force, along with an introduction to the Lund plane methodology, is provided in Chapters 2 and 3.

In Chapter 4 the experimental setup of the ALICE detector at CERN is described.

The analysis method, elucidated in Chapter 5, details the techniques used for studying jets and representing their internal structure.

Chapter 6 is dedicated to ensuring the quality and reliability of the data analyzed in this study, setting the stage for the results presented in Chapter 7.

2   Theoretical background

The Standard Model is a theory that describes the fundamental particles and three of the four known fundamental forces in the universe: the electromagnetic force, the weak nuclear force, and the strong nuclear force [1]. The gravitational force, described by General Relativity, is not included in the Standard Model due to the difference in how gravity is described and how it interacts with the other three forces, which are successfully unified by the Standard Model.

The Standard Model classifies the fundamental particles into fermions and bosons. Fermions are the building blocks of matter and they are divided into leptons and quarks. Bosons are instead the force carriers associated with the fundamental forces: photons (γ) carry the electromagnetic force, $W^{\pm}$ and Z^0 bosons carry the weak interaction, gluons carry the strong force, and the Higgs bosons are responsible for giving mass to the other elementary particles. Figure 1 gives a schematic overview of the Standard Model.

This thesis focuses on the strong force within the Standard Model.
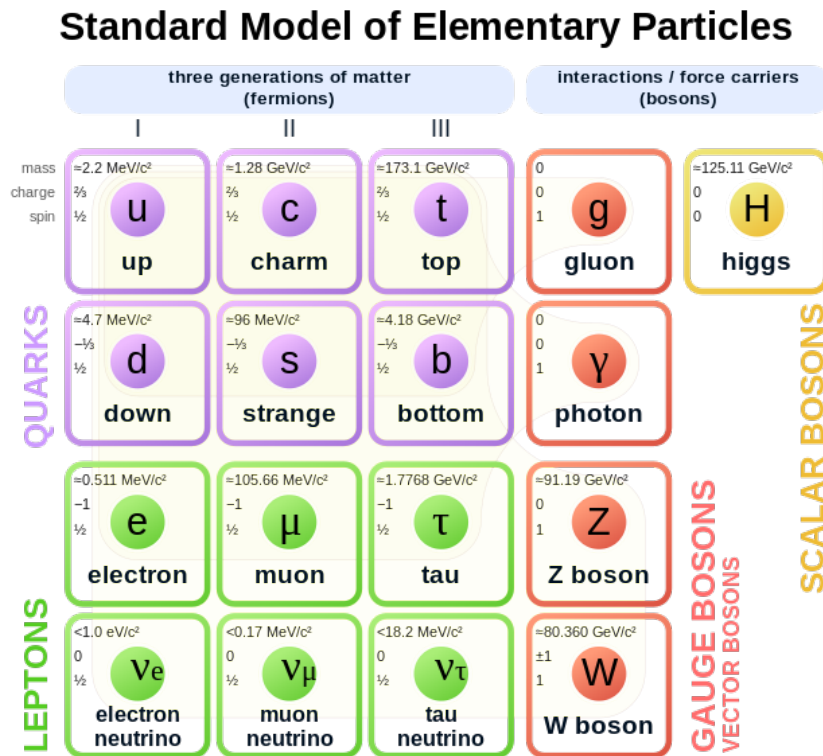
Figure 1: Standard Model of elementary particles: the 12 fundamental fermions and the 5 fundamental bosons. Brown loops indicate which bosons (red) couple to which fermions (purple and green) [2].

2.1   Quantum Chromodynamics

Quantum Chromodynamics (QCD) describes the strong interaction, responsible for binding quarks together forming hadrons, with gluons as mediators of this force.

QCD is a non-Abelian gauge theory, whose underlying gauge symmetry is SU(3) with the color charge as a locally conserved quantity [3][4]. The color charge is a type of charge

analogous to the electric one in electromagnetism, but existing in three states: red, green, and blue and their counterparts (rgb and $\overline{rgb}$).

Gluons are the mediators of the strong interaction, and the general SU(3) transformation predicts eight parameters, leading to the existence of eight massless gluons that govern the strong forces. The gluons do not only interact with color-charged quarks but also with themselves, making the strong force self-interacting. This is a unique feature of the strong force compared to the other fundamental forces.

The strong coupling constant α_s in QCD determines the strength of the strong force and it behaves in a much different way than the coupling constants in electromagnetism or gravity. In fact, while the other coupling constants are relatively stable across different energy scales, the strong coupling constant decreases as the energy scales, or the momentum transfers (Q^2), increase.

Thus, processes involving a large momentum (or energy) transfer, where α_s is small and so the strong force is weak, can be investigated via a perturbative approach (pQCD). This involves an expansion to higher orders in α_s, with only lower orders contributing significantly [5]. During these processes, as the strength of the strong interaction decreases, quarks and gluons start to behave as free particles. This behavior of the strong coupling constant is called asymptotic freedom.

On the contrary, for processes involving a low momentum (or energy) transfer, the perturbative approach of QCD breaks down, as higher orders become dominant [6]. In fact, the strong force becomes so strong that quarks are confined within hadrons. This phenomenon is called color confinement.

The dependence on the energy scale of the coupling strength in QCD can be described by the first-order approximated formula:

$$\alpha_s(Q^2) = \frac{12\pi}{(33 - 2n_f)\ln\left(\frac{Q^2}{\Lambda^2}\right)} \tag{1}$$

where:

- Q^2 is the energy scale;

- n_f is the number of quark flavours;

- Λ is the QCD scale parameter, which sets the scale at which the effects of the strong interaction become significant.

Experiments conducted at high energies have confirmed the predicted behavior of the strong force by observing α_s as a function of the momentum transfer Q, as illustrated in Figure 2.

2.2   Quark-gluon plasma

The quark-gluon plasma (QGP) is a unique state of matter where quarks and gluons are in a deconfined state, yet they interact strongly with each other. Thus, differently from normal hadronic matter, where quarks and gluons are confined within hadrons, in the QGP this confinement breaks down creating a strongly interacting deconfined state of matter.

Figure 3 illustrates the phase diagram of the QGP as well as the other states of matter under varying conditions of temperature T and baryon chemical potential μ_B. The latter
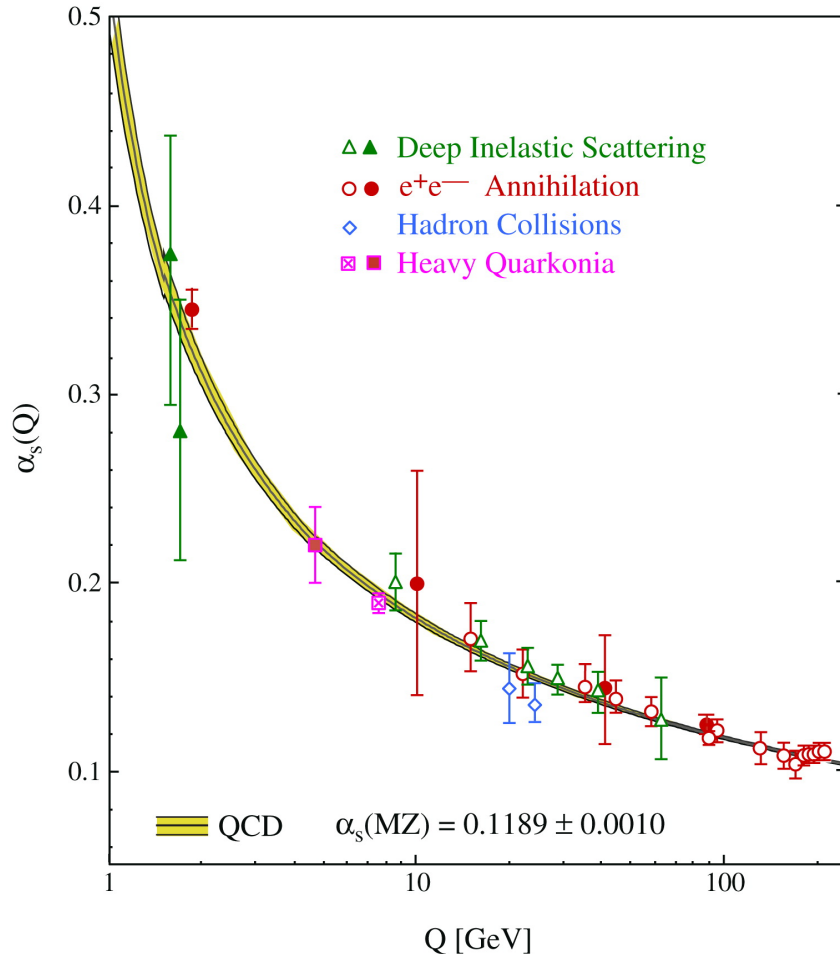
Figure 2: Summary of experimental measurements of α_s as a function of the energy scale Q [7].

quantity corresponds to the energy needed to increase the baryon number by one unit at fixed volume and entropy of the system and is proportional to the net baryon density of the system [5]. At low temperatures and low chemical potentials, matter exists in the hadronic phase, where quarks and gluons are confined within hadrons. The transition of matter into the QGP phase occurs either by increasing the temperature at low chemical potential (as in heavy-ion collisions) or by increasing the density at relatively lower temperatures. The endpoint of the first-order phase transition line separating the hadronic and QGP phases is called critical point. The existence and location of the critical point are subjects of ongoing research [8][9].

The quark-gluon plasma is an interesting phenomenon not only for its unique properties but also because it is believed that the universe was in this state of matter right after the Big Bang, before cooling down enough for quarks and gluons to condense into hadrons.

2.3   High-energy particle collisions

High-energy particle collisions are performed in particle accelerators, like the Large Hadron Collider (LHC) at CERN, with the aim of probing the structure of matter down to its most elementary constituents - quarks and gluons - and investigating the nature of
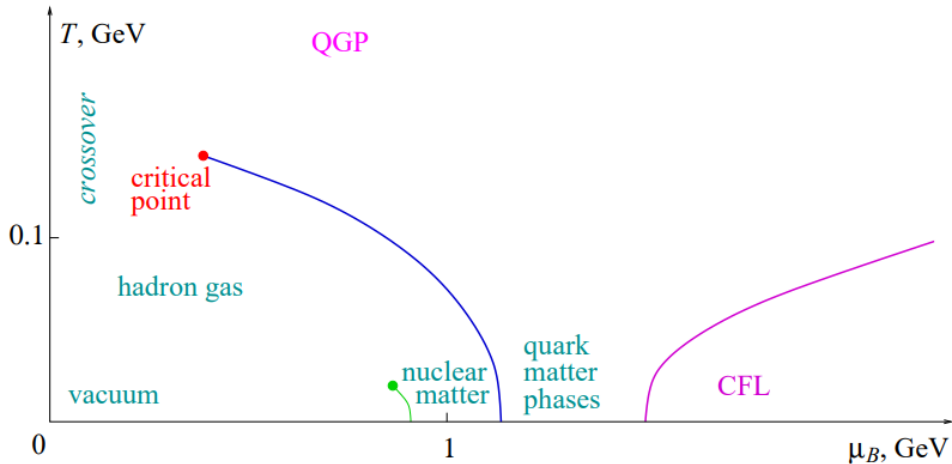
Figure 3: Schematic phase diagram of nuclear matter [10].

the fundamental forces.

In high-energy particle collisions, two or more particles, like protons or heavy ions, are accelerated to near the speed of light, reaching relativistic energies. These collisions are also called high-Q^2 processes because the energy scale Q^2 involved is large.

The energy scale is a measurement of the four-momentum transfer. Specifically, the four-momentum transfer q is defined as the difference between the four-momentum of the incoming particle p_1 and the four-momentum of the outgoing particle p_2:

$$q = p_2 - p_1 \tag{2}$$

where the four-momentum p of a particle is given by $p = (E, \vec{p})$, with E being the energy of the particle, and $\vec{p}$ the three-momentum vector.

The square momentum transfer q^2 is given by:

$$q^2 = (E_2 - E_1)^2 - (\vec{p_2} - \vec{p_1})^2 \tag{3}$$

where E_1 and E_2 are the energies before and after the collision, and $\vec{p_1}$ and $\vec{p_2}$ are the three-momentum vectors before and after the collision.

To ensure that q^2 is always positive, it is possible to define Q^2 in terms of q as follows:

$$Q^2 = -q^2 \tag{4}$$

Q^2 is a fundamental quantity that characterizes the energy scale involved in the collision. Specifically, high-Q^2 interactions involve a high energy and momentum exchange, implying that the interaction is probing very short distances within the proton, on the order of the size of quarks and gluons. This makes high-Q^2 processes particularly useful for studying the interactions of quarks and gluons and the dynamics of the strong force.

2.3.1   Proton-proton collisions

When high-Q^2 proton-proton collisions occur, the protons' constituents - quarks and gluons - interact via the strong force with a large momentum transfer. These interactions produce many new quarks and gluons.

The newly created partons undergo a series of radiative emissions and splitting, like gluon Bremmsstrahlung (a quark emits a gluon), gluon splitting (a gluon splits into two gluons or a quark-antiquark pair), and quark pair production (creation of quark-antiquark pairs). As the parton shower moves away from the collision point, the partons cannot remain free due to color confinement (see Subsection 2.1) and so they begin to fragment. In the fragmentation process, the energy of the free partons is converted into quark-antiquark pairs. Finally, the quark-antiquark pairs produced during fragmentation combine with each other and form hadrons. This process is known as hadronization.

The collimated stream of hadrons forming from the latest stages of the collision is called jet.

Figure 4 illustrates the main stages of a pp collision and the formation of jets.

The study of pp collisions is of great interest not only because they serve as a reference
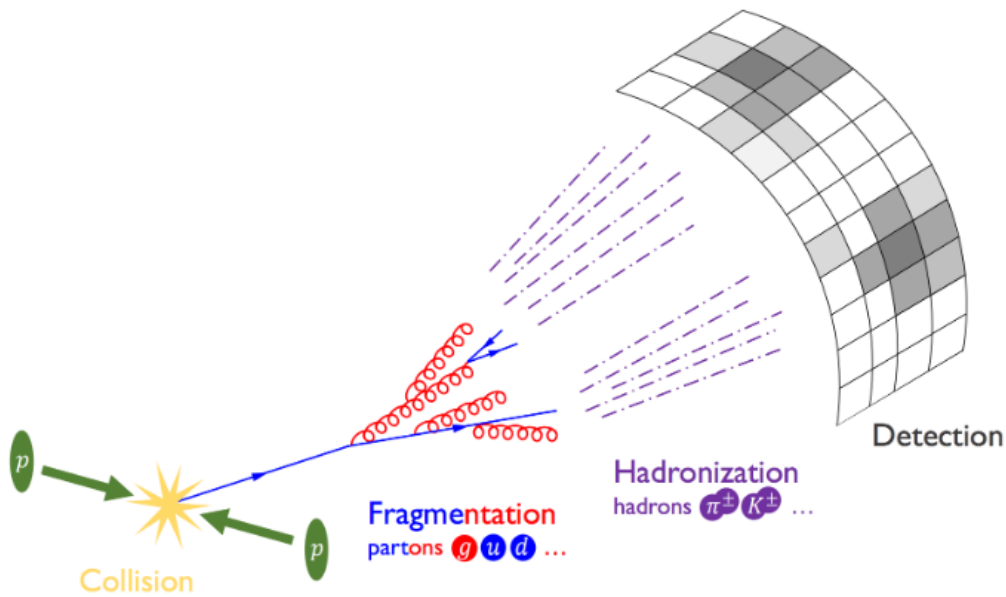

Figure 4: Schematic view of a proton-proton collision showing the evolution of the particles produced in the collision, which undergo fragmentation and hadronization before being detected [11].

point for heavy-ion collisions, but also because they enable to probe the substructure of protons and to measure the properties of their constituents.

2.3.2   Heavy-ion collisions

Heavy-ion collisions are of great relevance because they allow to recreate the quark-gluon plasma in the laboratory. In fact, the high energy at which these collisions occur generates temperatures and densities high enough to produce QGP.

Heavy ions, like lead (Pb), are accelerated to near the speed of light, reaching relativistic energies. At the moment of their collision, the energy density in the collision zone reaches extreme values far exceeding those inside a proton. This breaks down the protons and neutrons of the colliding ions into their constituent quarks and gluons.

Right after the collisions, there is a pre-equilibrium stage called color glass condensate (CGC) where gluons start to strongly interact.

Then, within a time $\tau = \tau_0 < 1\,\mathrm{fm}/c$, the system thermalizes, and the quark-gluon plasma forms.

Due to the expansion of the system, the plasma immediately starts to cool down and the temperature drops below the critical threshold of $T_C = 155\,\mathrm{MeV}$ where quarks and gluons start to recombine into hadrons. This process is called hadronization.

Subsequently, the system undergoes a chemical freeze-out, where inelastic collisions cease, and the relative abundances of different hadron species are fixed. This is succeeded by a kinetic freeze-out, where also elastic collisions eventually stop, and the particles' momenta are fixed. The particles then stream freely towards the detectors, where they are detected and analyzed.

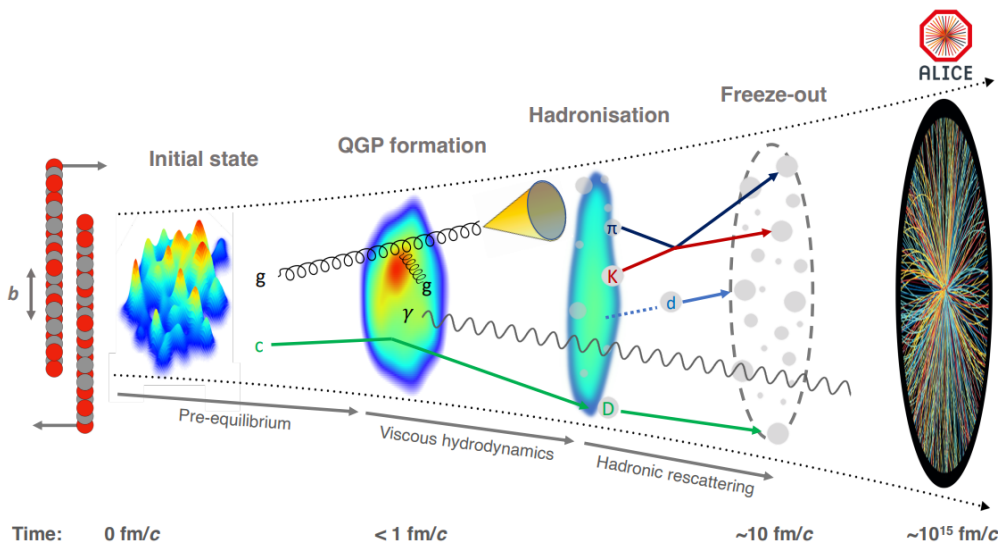Figure 5 shows the main stages of a relativistic heavy-ion collision.

Figure 5: Sketch of the different stages of a relativistic heavy-ion collision, featuring the initial pre-equilibrium stage, followed by the intermediate QGP phase, which terminates with the hadronization, the freeze-out, and the detection [5].

2.4   Jet quenching

In the early moments of a heavy-ion collision, high-energy quarks and gluons are produced through hard scattering processes. These partons typically fragment into jets as they move into the vacuum.

When the quark-gluon plasma is formed right after the collision, the partons produced from the collisions interact with the deconfined quarks and gluons in the QGP before fragmenting into jets. In these interactions, the energy of the partons is reduced mainly through two mechanisms: collisional energy loss and radiative energy loss.

Collisional energy loss refers to the loss of parton energy due to elastic scattering with the medium's constituents.

Radiative energy loss involves the bremsstrahlung emission of gluons due to the parton's acceleration in the color field of the medium.

As a consequence of these parton energy modifications, the parton showers passing

through QCD are different from those moving into the vacuum. This modification of the parton shower due to the presence of the medium is called jet quenching.

The energy loss occurring during the interactions between the partons from the collision and the QGP is sensitive to the density and the temperature of QGP. This makes jet quenching a useful probe for characterizing the properties of the QCD medium. Experimentally, the dynamics of this energy loss and the medium's response can be investigated through several observables, such as the suppression of high-energy jet yields, the modifications to jet shapes and structures, and the momentum differences between back-to-back jet pairs.

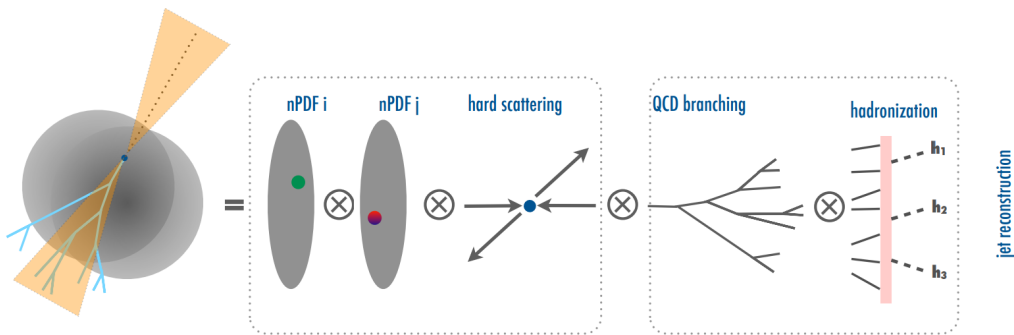The various stages of jet production in heavy-ion collisions are schematically shown in Figure 6.

Figure 6: The successive stages of jet production in the presence of a medium [12].

3 Lund plane

The Lund plane is a powerful tool to visualize the internal structure and evolution of jets [13] and it serves as a bridge between the study of jet quenching in heavy-ion collisions and the detailed understanding of jet fragmentation and hadronization processes.
There are several ways for representing jet emissions.

One simple way is to represent the particles inside the jets using segment lines. The particles' direction and scalar momentum are represented respectively by the direction and the length of the segment lines. Figure 7 shows a representation of two jets of particles, with the black line (a) being the primary particle, which initiated the jet, and the blue (b) and red (c) lines being the particles emitted inside the jet.

Another way to represent the jet substructure is via the Lund diagram. The Lund

Figure 7: A possible representation of the particles inside the jet using segment lines [13].

diagram is a theoretical representation of the phase-space of emission in jets [14] where each point in the plane corresponds to a specific state in the fragmentation process of a parton. In a Lund diagram, the phase space accessible for particle emissions is represented as a triangle within a two-dimensional logarithmic plane, with the axes being the emission angle Δ and the transverse momentum k_t (or the fraction of the longitudinal momentum of a parton z) of an emission 2 with respect to its emitter 1, defined as:

$$\Delta \equiv \Delta_{12} = \sqrt{(\eta_1 - \eta_2)^2 + (\phi_1 - \phi_2)^2}, \tag{5}$$

$$k_t \equiv p_{\perp 2}\Delta_{12}, \quad z \equiv \frac{p_{\perp 2}}{p_{\perp 1} + p_{\perp 2}}. \tag{6}$$

where η and ϕ are respectively the pseudorapidity and azimuthal angle of a particle.
Every emission, in turn, generates additional phase space (in the form of a new triangular area) for subsequent emissions.
In Figure 8 the black triangle (a) represents the primary phase space. Each emitted particle (b) and (c) is represented as a point at the appropriate (Δ, k_t) coordinate on the primary phase space and has its own phase-space region, represented by the colored triangles, called secondary Lund triangles.

The primary Lund plane is a simplified representation that contains only the positions of the emissions from (a), but no information about what further secondary emissions may have been produced, as shown in Figure 9.

3.1 Lund plane density

The simplest analysis that can be performed on the primary Lund plane is to examine the average density of points per jet and per unit area in the (Δ, k_t) plane [13][15], defined as:

$$\rho(\Delta, k_t) = \frac{1}{N_{\text{jets}}} \frac{\mathrm{d}^2 n_{\text{emissions}}}{\mathrm{d}\ln\frac{1}{\Delta}\,\mathrm{d}\ln k_t} \tag{7}$$
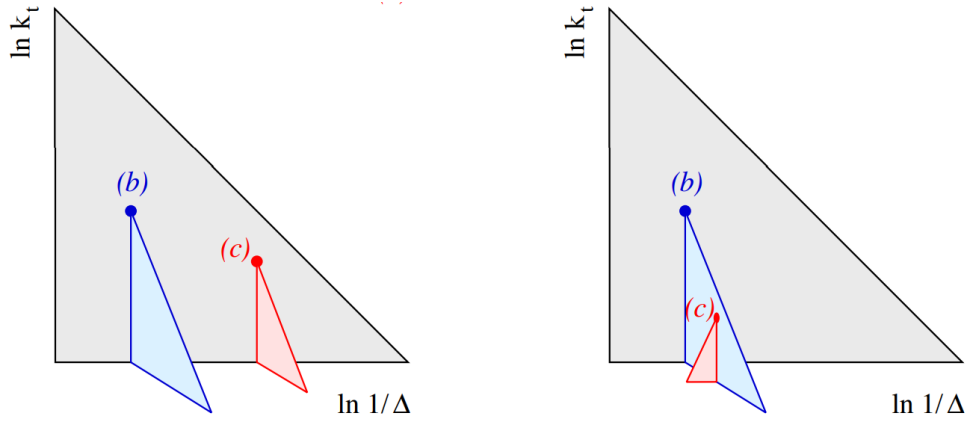
Figure 8: Jet substructure representation via the Lund diagram. On the left, both (b) and (c) are emitted by (a), so their triangles are both associated with the primary phase-space. On the right, particle (c) is emitted by particle (b), so the red triangle is associated with the blue one, and not directly with the primary phase-space [13].
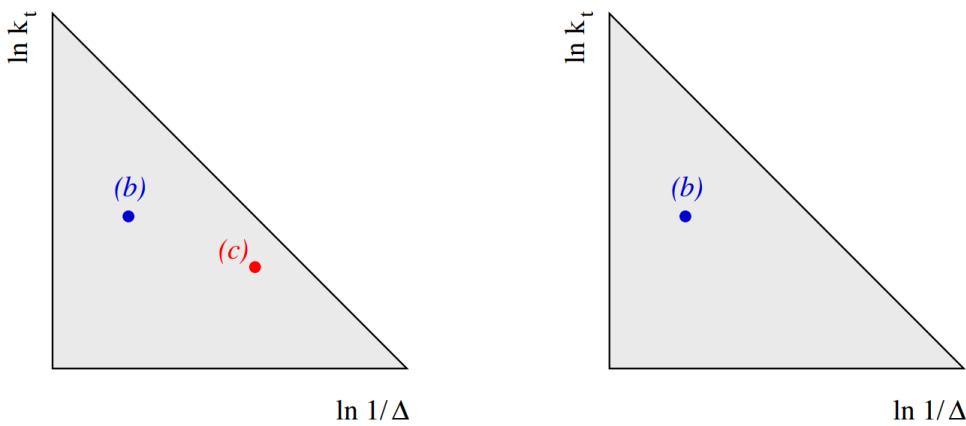

Figure 9: Jet substructure representation via the Primary Lund plane. On the left, both (b) and (c) are represented as points in the plane since both particles are primarily emitted from (a). On the right, only (b) is primarily emitted by (a), while (c) is a secondary emission, so it is not represented in the primary Lund plane [13].

where N_{jets} is the total number of jets and $n_{\text{emissions}}$ is the total number of emissions in the selected interval of the jet's transverse momentum.

Alternatively, this can be defined in terms of z as:

$$\tilde{\rho}(\Delta, z) = \frac{1}{N_{\text{jets}}} \frac{\mathrm{d}^2 n_{\text{emissions}}}{\mathrm{d} \ln \frac{1}{\Delta} \, \mathrm{d} \ln \frac{1}{z}}. \tag{8}$$

Given an ensemble of many jets, it is possible to determine the average Lund plane density at leading order in the soft and collinear limits, i.e. the particles are emitted with low energy and at a direction close to their emitter:

$$\rho^{\text{LO},i}_{\text{soft-coll.}}(\Delta, k_t) = \frac{2\alpha_s C_i}{\pi}, \tag{9}$$

where C_i is the Casimir of the hard parton of flavour i initiating the jet ($C_i = C_A$ for a gluon-initiated jet and $C_i = C_F$ for a quark-initiated jet) and α_s is the strong coupling constant. Thus, from the Lund plane density, it is possible to extract information

regarding the running of the strong coupling constant.

However, beyond leading order, the average Lund plane density becomes logarithmic:

$$\rho_{\text{soft-coll.}}^{\text{NLO},i}(\Delta, k_t) = \frac{2C_i}{\pi} \alpha_s^{n+1} \ln^m(\Delta) \ln^{n-m}(p_\perp/k_t),\tag{10}$$

assuming that the order is $n + 1$ and that $0 \leq m \leq n$.

To calculate the whole set of logarithmic contributions to $\rho(\Delta, k_t)$, the corrections coming from different physical phenomena have to be taken into account:

1. Running coupling corrections

2. Hard-collinear effects

3. Soft emissions at large or commensurate angles

3.1.1 Running coupling corrections

As already said in the Subsection 2.1, the strong coupling constant behaves differently at different momentum transfers (see Figure 2).

In order to take this into account, the scale of the running coupling in the Lund plane density is simply set by the transverse momentum of the emission:

$$\rho_{rc,i}(\Delta, k_t) = \frac{2\alpha_s(k_t)C_i}{\pi}\tag{11}$$

A more accurate study of the running coupling correction requires the calculation of 2-loops running coupling, which incorporates higher-order corrections. The 2-loop running coupling in the Catani-Marchesini-Webber (CMW) scheme results to be:

$$\begin{aligned}
\alpha_s(k_t) =& \frac{\alpha_s}{1 - 2\alpha_s\beta_0 \ln\left(\frac{p_\perp R}{k_t}\right)} - \frac{\beta_1\alpha_s^2}{\beta_0} \frac{\ln\left(1 - 2\alpha_s\beta_0 \ln\left(\frac{p_\perp R}{k_t}\right)\right)}{\left[1 - 2\alpha_s\beta_0 \ln\left(\frac{p_\perp R}{k_t}\right)\right]^2} \\
&+ \frac{K}{2\pi} \frac{\alpha_s^2}{\left[1 - 2\alpha_s\beta_0 \ln\left(\frac{p_\perp R}{k_t}\right)\right]^2}
\end{aligned}\tag{12}$$

with

$$\beta_0 = \frac{11C_A - 2n_f}{12\pi}, \beta_1 = \frac{17C_A^2 - 5C_A n_f - 3C_F}{24\pi^2}, K = \left(\frac{67}{18} - \frac{\pi^2}{6}\right)C_A - \frac{5}{9}n_f.\tag{13}$$

3.1.2 Hard-collinear effects

Equation 11 assumes that the primary branch keeps the flavour of the initial parton [15]. However, in reality, the phenomena of hard and collinear branchings have significant effects on the dynamic of the process.

Hard branches refer to the high-momentum transfer splittings that occur during the initial stages of particle collisions, leading to the production of high-energy particles. On the other hand, collinear branchings describe the process where partons split into pairs in a direction almost parallel to their original path.

The effects of these branchings are:

- The flavour of the quark of the harder branch - which can be $q \to qg$ or $g \to q\bar{q}$ - can change

- The leading parton can lose some of its transverse momentum

To apply this correction, the Lund plane density is multiplied by the probability density of having a leading parton of flavour j, carrying a longitudinal fraction x, when the primary Lund declustering procedure has reached an angular scale Δ:

$$\rho_{\text{coll},i}(\Delta, k_t) = \sum_j \int_0^1 dx\, p(x, j|i, t_{\text{coll}}(\Delta; \Delta_0, \mu)) \left(\frac{xp_\perp \Delta}{2C_j k_t}\right) P_j \left(\frac{k_t}{xp_\perp \Delta}\right) \rho_{\text{rc},j}(\Delta, k_t), \quad (14)$$

where P_j is the DGLAP splitting function. Equation 14 includes the effects of the flavour changes and the distribution of the longitudinal momentum fraction of the leading parton [15].

3.1.3 Soft emissions

Partons can emit other partons as they move. If the emitted parton has low energy, the emission is called soft. Soft emissions have several effects:

- At $O(\alpha_s)$, soft parton radiation is a coherent sum from all hard coloured partons, and not just one.

- At higher orders, a soft parton can lead to subsequent soft emissions at commensurate angles. Additionally, for two or more partons at similar angles, jet clustering's role in categorizing each parton as primary or secondary Lund emission becomes crucial.

In the large-N_C limit, taking a dijet process with two incoming and two outgoing partons, this can be represented as a sum over various partonic channels, each being a weighted sum of distinct color flows:

$$\rho_{\text{soft}}(\Delta, k_t) = \sum_{i \in \text{jet flavours}} f_i \rho_{\text{soft},i}(\Delta, k_t), \quad (15)$$

where f_i is the relative fraction of parton jets.
It is possible to expand $\rho_{soft,i}$ as a series in α_s:

$$\rho_{\text{soft},i}(\Delta, k_t) = \sum_{n=1}^{\infty} \alpha_s^n \rho_{\text{soft},i}^{(n)}(\Delta, k_t), \quad (16)$$

At single-logarithmic accuracy:

$$\alpha_s^n \rho_{\text{soft},i}^{(n)}(\Delta, k_t) \propto \alpha_s^n \ln^{n-1}\left(\frac{p_\perp \Delta}{k_t}\right), \quad (17)$$

At fixed α_s^2 order, for a quark/gluon emitted at commensurate angles from the direction of the original particle:

$$\alpha_s^2 \rho_{\text{soft}}^{(2)} = 0.323066 \left(\frac{2\alpha_s}{\pi}\right)^2 C_F(C_F - C_A) \ln\left(\frac{k_t}{p_\perp \Delta}\right) \quad [\text{quark}], \quad (18)$$

$$\alpha_s^2 \rho_{\text{soft}}^{(2)} = 0 \quad [\text{gluon}], \tag{19}$$

while, at large angles from the direction of the original particle, another source of logarithmic enhancement intervenes:

$$\alpha_s^n \ln^m \left(\frac{p_\perp R}{k_t} \right) \ln^p \left(\frac{R}{R - \Delta} \right), \quad \text{with } m \leq n - 1, \, p \leq n - 1. \tag{20}$$

At all-order, the correction to the Lund plane density is given by an extra density factor which encodes all the soft emission effects:

$$\rho_{\text{soft}} \left(\Delta, t_{\text{soft}}(k_t, p_\perp \Delta; \mu) \right) \tag{21}$$

with

$$t_{\text{soft}}(k_t, p_\perp \Delta; \mu) = \int_{k_t}^{p_\perp \Delta} \frac{dq_{t1}}{q_{t1}} \alpha_s(q_{t1}) \tag{22}$$

3.1.4 Full resummed results

Summing up all the contributions coming from the running of the strong coupling constant, the collinear effects - including flavour changes, splitting functions and the momentum of the leading parton - as well as the soft-gluon emissions to all orders - including large-angle contributions and clustering effects for emissions at commensurate angles -, the full result is:

$$\rho_{\text{resum}}(\Delta, k_t | p_\perp) = \sum_{i,j=q,g} f_i(\mu_F) \int_0^1 dx \, p(x, j | i, t_{\text{coll}}(\Delta_0, \Delta; \mu_R) \frac{\alpha_s(\xi_K k_t)}{\pi}) \\ \left[\frac{P_j(z \equiv k_t/(x p_\perp \Delta))}{2 C_j / z} \right] \rho_{\text{soft},j} \left(\Delta, t_{\text{soft}}(x p_\perp \Delta, \xi_Z k_t; \mu_R) \right) \tag{23}$$

where:

- the factor $\frac{\alpha_s(\xi_K k_t)}{\pi}$ comes from the running coupling correction (see Section 3.1.1);

- the factor $p(x, j | i, t_{\text{coll}})$ encodes the probability for the leading parton to have a momentum fraction x and a flavour j, starting from a jet of flavour i (with initial fraction f_i) computed in the collinear limit. Similarly, the factor $z P_j/(2 C_j)$ accounts for the collinear structure associated with an observed Lund plane emission at finite z [15] (see Section 3.1.2);

- the factor ρ_{soft} encodes the soft emission correction (see Section 3.1.3);

- the scales $\mu_R = \xi_R p_\perp R$, $\mu_F = \xi_F p_\perp$ and the factors ξ_K and ξ_Z probe the scale uncertainties.

Figure 10 shows how to calculate the density at a point (Δ, k_T) (the black dot) in the Lund plane using Equation 23. First, collinear effects are resummed down to the angle Δ (blue line), then soft emission at commensurate angles between $x p_\perp \Delta$ and k_T are resummed (red line). This means that, at large angles, collinear effects can be neglected while, at small angles, collinear effects contribute to the density calculation and the soft emission contribution to the density depends only on the jet flavour.

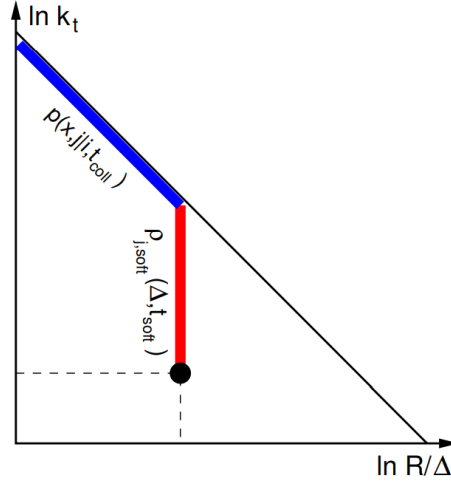The study of the Lund plane density is of great relevance not only because it allows

Figure 10: Schematic representation of Equation 23. The Lund plane density is obtained by first resumming collinear effects down to the angle Δ and then soft emissions at commensurate angles between $xp_\perp\Delta$ and k_T [15].

to extract information on the strong coupling constant, but also because it highlights the effect coming from several physical phenomena occurring in jet emission.

Several studies have been performed with the aim of representing the jet substructure in the Lund plane and studying the effect of the different contributions to the density. Notably, the ATLAS Collaboration has conducted measurements of the unfolded Lund plane for very high p_T jets [16], while the ALICE Collaboration has extended these observations to include jets with lower transverse momenta [17].

This thesis provides the first measurement of the Primary Lund plane for high p_T jets detected by the ALICE detector during the LHC Run3 in 2022 from proton-proton collision.

4   Experimental setup: ALICE detector

ALICE (A Large Ion Collider Experiment) is one of the major experiments at the Large Hadron Collider (LHC) at CERN, the European Organization for Nuclear Research [18].

The LHC is the world's largest and most powerful particle accelerator consisting of a 27 km ring beneath the France–Switzerland border near Geneva. Currently, during Run 3, the LHC accelerates and collides proton bunches at a center of mass energy of 13.6 TeV and heavy-ion (Pb) bunches at 5.36 TeV per nucleon pair [19]. The protons or ions are accelerated in two rings in opposite directions and are maintained in their trajectories by the use of superconducting magnets, which generate a magnetic field of 8.3 Tesla.

The LHC hosts 4 major experiments: ATLAS (A Toroidal LHC Apparatus), CMS
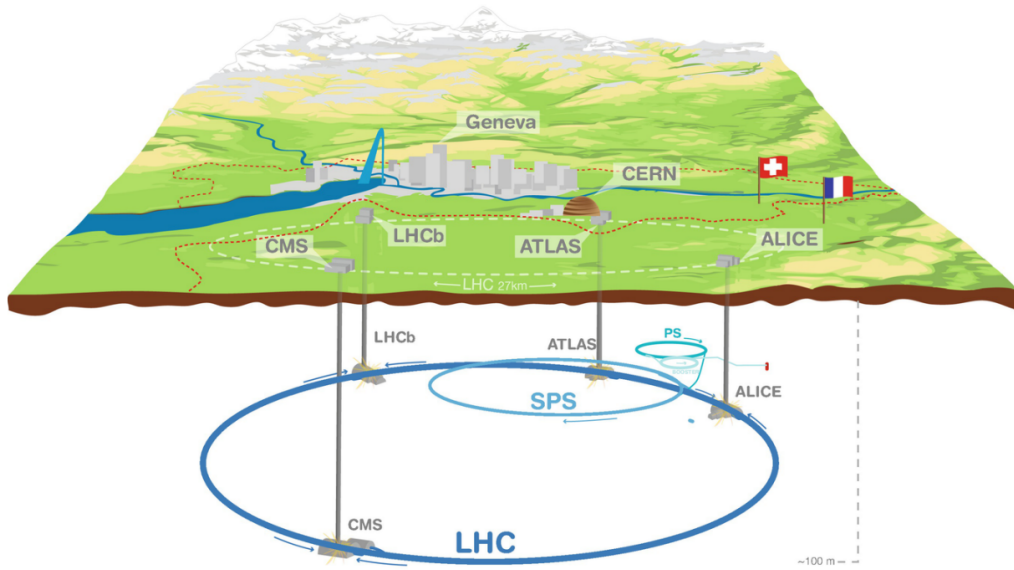
Figure 11: Overall view of the Large Hadron Collider, including the ATLAS, CMS, LHCb, and ALICE experiments.[20]

(Compact Muon Solenoid), LHCb (Large Hadron Collider beauty), and ALICE.

Situated at one of the LHC's four particle collision points, ALICE is specifically devoted to QGP studies and it is designed to analyze the various stages of the evolution of the heavy-ion collisions, specifically Pb-Pb collisions, from the initial state to the QGP phase and to the transition to hadronic matter. This study is critical for understanding the formation of particles that constitute the matter of the universe. This is achieved by tracking particles produced within the hot, expanding volume, which survive long enough to interact with the detector layers around the collision area.

At the same time, data from proton-proton collisions are collected and analyzed, serving as a reference for nucleus-nucleus reactions but also for specific QCD studies [5] (see Section 6).

In order to be able to identify all the produced particles and their charge, the experiment has to rely on a set of 18 detectors, designed to provide detailed information about particle mass, velocity, and electric charge, enabling comprehensive particle identification in these complex collision environments.

Recently, the ALICE apparatus has undergone a major update and the ALICE 2 version has recently started collecting data of the Run 3 of the LHC.

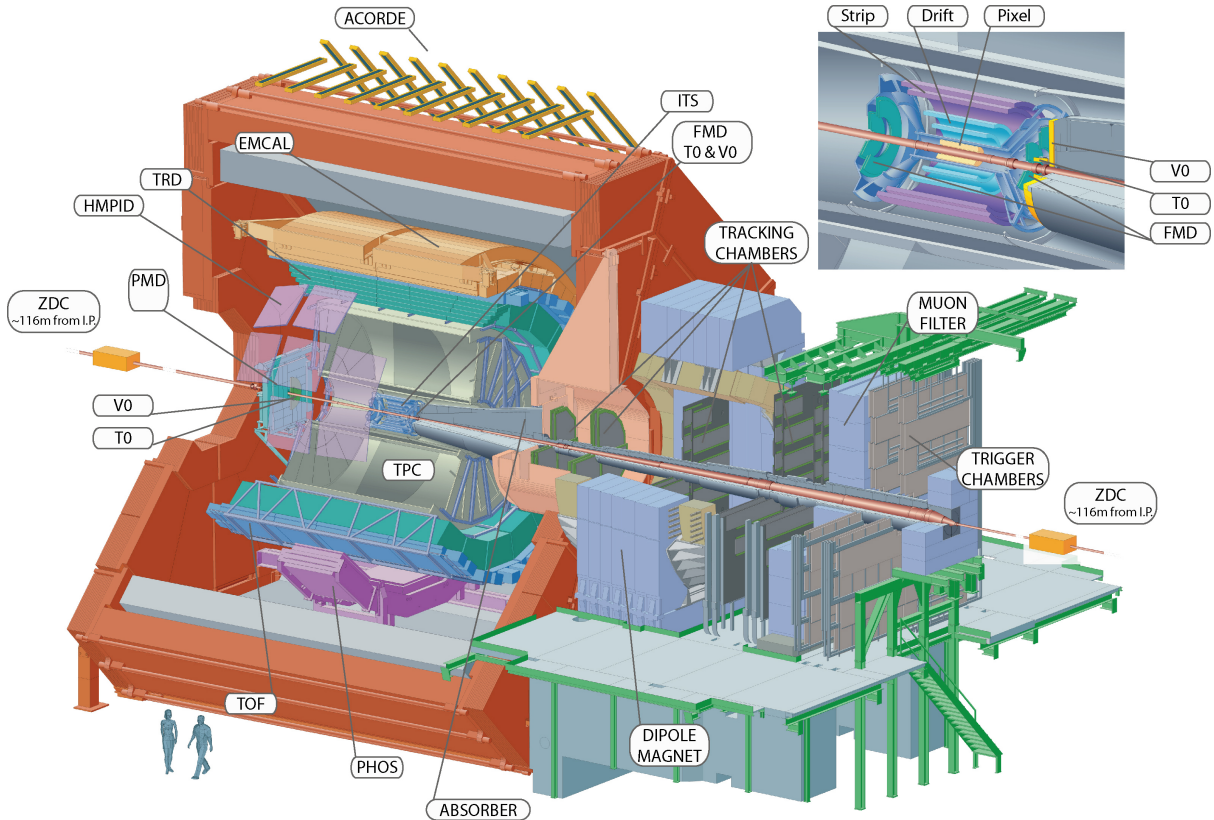An overview of the main components of the ALICE detector is shown in Figure 12.

Figure 12: Main components of the ALICE detector.[21]

4.1   Barrel Tracking

The barrel detectors of the ALICE experiment (TPC, ITS and TRD) are used to track all the particles emanating from the interaction point. These detectors, situated in a 0.5 Tesla magnetic field, enable precise tracking of particle trajectories and momentum determination.

4.1.1   TPC

The Time Projection Chamber (TPC) is the main particle device tracking in the ALICE detector. It is a large cylindrical gas-filled volume able to detect charged particles by measuring the ionization they cause in the gas. As these particles traverse the TPC, they ionize the gas molecules, releasing electrons. These electrons are drifted towards the end plates of the TPC by an electric field. The position where they hit the end plates, combined with the drift time, provides a 3D image of the particle tracks.

4.1.2   ITS

The Inner Tracking System (ITS) of the ALICE detector is able to identify the precise location where the decay of short-living particles occurs, which usually is located near the collision point. It consists of six cylindrical layers of silicon detectors, each providing high-resolution measurements.

The location close to the interaction point allows the precise reconstruction of the vertices of particle collisions and the identification of particles containing heavy quarks by their decay signatures.

4.1.3   TRD

The Transition Radiation Detector (TRD) is designed to identify electrons and positrons using the principle of transition radiation. This occurs when charged particles, specifically high-energy electrons, pass through layers of materials with different dielectric constants, which can lead to the emission of an X-ray. The TRD detects these X-rays, enabling the discrimination of electrons from other particles. This capability is crucial for particle identification.

4.2   Particle Identification

The ALICE detector is able to perform particle identification through the determination of each particle's mass and charge.
Mass is inferred from momentum and velocity measurements, with momentum and charge signs derived from track curvature in a magnetic field. Velocity is calculated using methods based on time-of-flight, ionization, transition radiation, and Cherenkov radiation.

The Time-Of-Flight (TOF) detector, the High Momentum Particle Identification Detector (HMPID), and the Muon Spectrometer are components within ALICE able to identify different particles, each employing specific techniques suitable for various momentum ranges and particles types.

4.3   Calorimeters

The calorimeters of the ALICE detector are used for measuring the energy of particles and determining whether they have electromagnetic or hadronic interactions. These measurements in ALICE are destructive, meaning particles like photons, electrons, and positrons fully expend their energy in the calorimeter, forming electromagnetic showers.

Calorimeters like the Photon spectrometer (PHOS) and the Electro-Magnetic Calorimeter (EMCal) are essential for these measurements, with PHOS providing high precision and EMCal offering broader coverage and the capability to analyze jets, revealing information about the early stages of particle collisions.

5   Analysis method

This thesis aims to examine the jet's internal structure making use of the Primary Lund plane. Before delving into the Primary Lund plane representation of the jet's substructure, several intermediate steps are required. Initially, the collimated spray of particles detected by the ALICE detector must undergo reconstruction, followed by the reclustering of the jet constituents.
The following Subsections provide a detailed description of the intermediate steps from jet detection to the analysis of jet substructures.

5.1   Jet reconstruction

In order to probe the jet substructures, the first step is to reconstruct the jets produced in the high-energy particle collisions by identifying the jet candidates [22].
Specific jet algorithms are able to cluster the detected particles into jets. For the data analyzed in this thesis, jets detected by ALICE are firstly reconstructed using the anti-k_T algorithm in `FastJet` [23].
        The anti-k_T algorithm is a sequential recombination algorithm that groups particles into jets based on their transverse momenta.
The distance between two particles in an event is defined as:

$$d_{ij} = \min\left(k_{Ti}^n, k_{Tj}^n\right) \frac{\Delta_{ij}^2}{R^2} \tag{24}$$

where $\Delta_{ij}^2 = (\eta_i - \eta_j)^2 + (\phi_i - \phi_j)^2$ is the angular separation, with η and ϕ being respectively the pseudorapidity and the azimuthal angle, R is the radius that sets the size of the jet and k_T is the transverse momentum of the particle.
The distance between the particle i and the beam B is defined as follows:

$$d_{iB} = k_{Ti}^n \tag{25}$$

For the anti-k_T algorithm, $n = -2$ and so Equations 24 and 25 becomes:

$$d_{ij} = \min\left(\frac{1}{k_{Ti}^2}, \frac{1}{k_{Tj}^2}\right) \frac{\Delta_{ij}^2}{R^2} \tag{26}$$

$$d_{iB} = \frac{1}{k_{Ti}^2} \tag{27}$$

        The algorithm proceeds by identifying the smallest distance between d_{ij} and d_{iB}. If the smallest distance is d_{ij}, then the particles i and j are combined into a single particle by summing up their four-momenta. If the smallest distance is d_{iB}, then the particle i is considered a final jet, and it is removed from the list of particles. This process is repeated until all particles are assigned to jets.
        As a consequence of the inverse proportionality of the distance to the transverse momentum, the clustering sequence tends to cluster softer particles (low k_T) around harder particles (high k_T), effectively building jets from the inside out, with the hardest particles at their cores, and producing jets with a stable circular area.
Figure 13 displays jet reconstructions through the anti-k_T algorithm from simulated events.
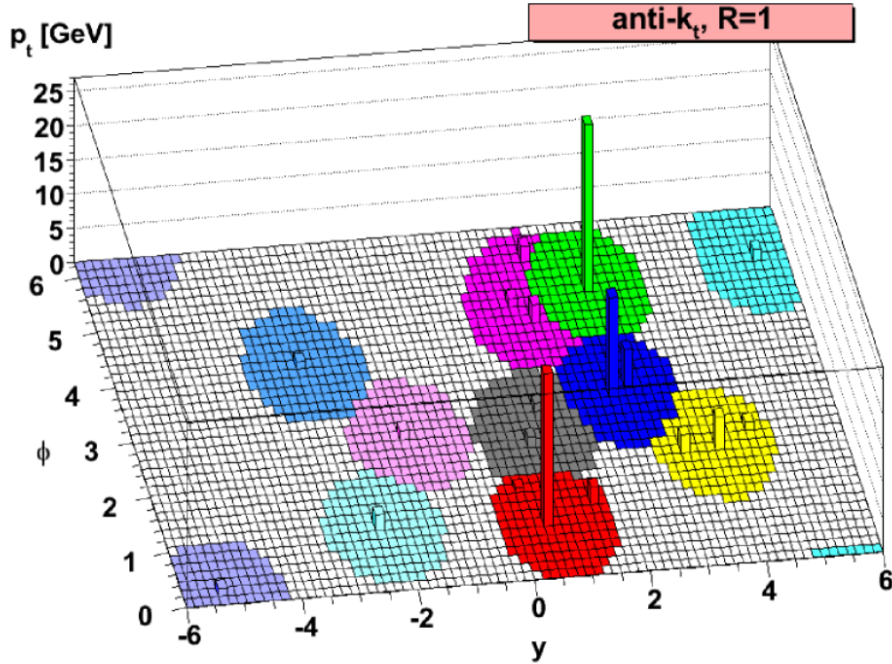
Figure 13: Event display of reconstructed jets from simulated events, assuming $R=1$, using the anti-k_T algorithm [23].

The advantages of using this algorithm are that it is infrared and collinear safe, meaning that it is insensitive to the addition of soft particles and to the collinear splitting of particles. In addition, the parameter R provides a simple way to set the size of the jets, making the algorithm flexible for different analyses.

5.2   Jet reclustering

Once all the detected particles have been clustered into jets and the jets have been clearly identified, their constituents can be re-clustered using the Cambridge/Aachen (C/A) algorithm. This allows for a detailed examination of the internal structure of these jets.

The C/A algorithm in `FastJet` [24] clusters particles into jets based on their angular separation rather than their transverse momentum.

For the C/A algorithm, $n = 0$, thus Equations 24 and 25 becomes:

$$d_{ij} = \frac{\Delta_{ij}^2}{R^2} \tag{28}$$

$$d_{iB} = 1 \tag{29}$$

The clustering sequence proceeds in the identification of the smallest distance between d_{ij} and d_{iB} as in the anti-k_T algorithm. However, the C/A algorithm relies only on the angular distance between the particles, with no k_T weighting at all. This makes it particularly sensitive to the geometric distribution of particles in a jet, which is useful for analyzing the jet's substructure.

Figure 14 displays jet reclustering through the C/A algorithm from simulated events.
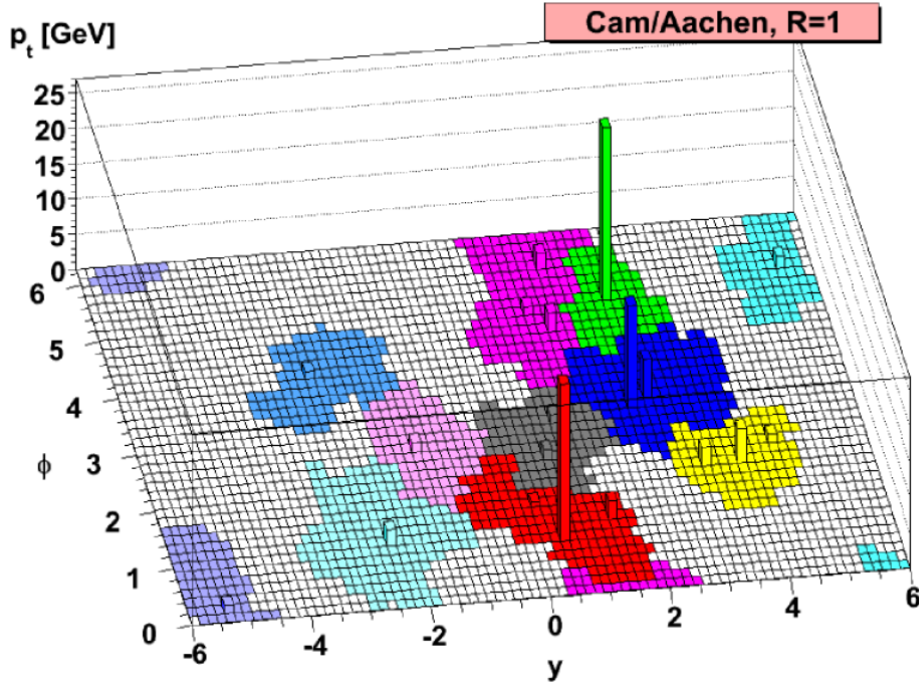
Figure 14: Event display of reclustered jets from simulated events, assuming R=1, using the C/A algorithm [23].

5.3   Jet declustering and jet substructure representation in the Lund plane

After clustering particles into jets and subsequently re-clustering the jet constituents, the next phase involves iteratively de-clustering the jet and populating the primary Lund plane (see Section 3). This process begins with j, which represents the fully re-clustered jet, and involves the following steps [15]:

1. Undo the last step of clustering: $j \rightarrow j_1 + j_2$, taking j_1 to be the harder branch, i.e. the branch that carries the most momentum (or energy):

$$p_{\perp 1} > p_{\perp 2}$$

2. Record the properties of the branching $T \equiv \{k_t, \Delta, z, \ldots\}$ defined as

$$\Delta \equiv \Delta_{12} = \sqrt{(\eta_1 - \eta_2)^2 + (\phi_1 - \phi_2)^2}, \tag{30}$$

$$k_t \equiv p_{\perp 2} \Delta_{12}, \tag{31}$$

$$z \equiv \frac{p_{\perp 2}}{p_{\perp 1} + p_{\perp 2}}. \tag{32}$$

with Δ being the angular separation between the jet's constituents, k_T the transverse momentum, and z the momentum fraction carried by one of the constituents relative to the total momentum of the two constituents, where η and ϕ denote the pseudorapidity and azimuthal angle of a particle:

$$y = \frac{1}{2} \ln \frac{E + p_z}{E - p_z}, \quad \phi = \arctan\left(\frac{p_y}{p_x}\right)$$

3. Redefine $j \leftarrow j_1$ and iterate following the harder branch.

The iteration stops when j can no longer be de-clustered, giving an ordered list of tuples:

$$L_{\text{primary}} = \left\langle T^{(1)}, \ldots, T^{(i)}, \ldots, T^{(n)} \right\rangle .$$

Each tuple in the list is represented as a point in the primary Lund plane, which is constructed using the code available within the ALICE Analysis framework [25], which makes use of `fastjet-contrib` [26].

The Lund plane is represented both in the $(\Delta, \, k_T)$ and in the $(\Delta, \, z)$ planes. A common choice for the horizontal axis of the Lund plane is the angular separation θ between the leading and subleading prong, defined as:

$$\theta = \frac{R}{\Delta R} \tag{33}$$

where R is the jet resolution parameter, which sets the radius of the jet in the $(\eta, \, \phi)$ space. A conventional choice is to set $R = 0.4$.

6   Data samples and quality assurance

Before delving into the Primary Lund plane analysis, it is of great importance to ensure the integrity and reliability of the data. As such, track quality assurance is a preliminary step in this thesis.

The focus of this study goes to the data from proton-proton collisions recorded by the ALICE detector during the LHC Run3 in 2022 at a collision energy of 13.6 TeV. Specifically, the datasets of interest are: `LHC22_pass4_highIR_sampling` (high interaction rate runs of the 2022 pp data-taking campaign) and `LHC22_pass4_lowIR` (low interaction rate runs of the 2022 pp data-taking campaign).

In this analysis, the LEGO trains [27] reported in Table 1 have been used and monitored via the MonALISA framework [28].

Each train has been run using 3 different configurations for the track parameters: a default configuration given by the `GlobalTracks` track selection, a loose configuration using cuts 20% looser than the default ones, and a tight configuration using cuts 20% tighter than the default ones. Table 2 shows the different cuts applied to some tracks observables.

The reason why cut variations have been performed is because, by varying the cuts around the nominal values, it is possible to evaluate the sensitivity of the results to the selection criteria. In addition, it is possible to gain a deeper understanding of the detector's efficiency and resolution, as well as of the performance of the track reconstruction algorithms under different conditions.

In addition to applying specific cuts on the track parameters, event selection and track selections are applied to the data, then quality assurance is performed.

Train run	Dataset	Production
175135	`LHC22_pass4_highIR_sampling`	`LHC22m_apass4,`
		`LHC22o_apass4,`
		`LHC22t_apass4,`
		`LHC22r_apass4,`
		`LHC22p_apass4,`
		`LHC22o-test_apass4`
174348	`LHC22_pass4_lowIR`	`LHC22f_apass4,`
		`LHC22m_apass4_lowIR,`
		`LHC22q_apass4_lowIR,`
		`LHC22o_apass4_lowIR,`
		`LHC22r_apass4_lowIR`

Table 1: Train run and datasets

6.1   Event selection

Event selection is the process of choosing collision events that meet specific criteria. This analysis uses `sel8` as the event selection criterion, which is based on timing information provided by the FT0 detector.

The FT0 is a detector component in ALICE that provides precise timing information

	Tight cuts	GlobalTracks	Loose cuts
MinNCrossedRowsTPC	80	70	65
MinNCrossedRowsOver FindableClustersTPC	0.9	0.8	0.6
MaxChi2PerClusterTPC	2	4	6
MaxChi2PerClustersITS	32	36	40
MaxDcaXY	0.1	0.25	0.5
MaxDcaZ	1	2	3

Table 2: Cut variation applied to several track observables

for collision events. This timing information is crucial for synchronizing the detected events with the bunch crossings, i.e. the moment of intersection between groups of protons in the accelerator, which potentially lead to collisions.

The `sel8` condition is a predefined standard event selection criterion that ensures that the recorded collisions occur close in time to the filled bunch crossings. For each reconstructed collision event (or vertex), the timing information is used to associate it with a specific bunch crossing: only collisions that are temporally aligned with a bunch crossing and pass this compatibility check are included in the analysis.

This condition is essential for associating each collision with the correct bunch crossing and for distinguishing between real collision events and background noise or events associated with empty bunch crossings.

In addition to this event selection, also a vertex selection is performed.
The primary vertex is the point on the beam axis z where the collision occurs. In this analysis, only events whose primary vertex is within $|z_{\text{vertex}}| < 10$ cm along the beam axis are selected.

This condition ensures the quality of the analyzed data, as events with vertices within the specified range are more likely to be accurately reconstructed, leading to higher-quality data.

6.2   Track selection

Track selection is the process of choosing those particle tracks that meet a specific criterion among many tracks detected in each event.
In this analysis, specific criteria are used for identifying and selecting particle tracks.

First of all, the track acceptance is $|\eta| < 0.9$ and $0 < \phi < 2\pi$ and the jet's transverse momentum is between 0 and 200 GeV/c, with a focus on high jet's transverse momentum.

In addition, this analysis accepts those global tracks that have hits in any one of all seven ITS layers. Global tracks refer to the trajectories of charged particles reconstructed using information and integrating signals and hits from different detector components. Only global tracks that interact with any part of the ITS are selected in this analysis. This criterion is encapsulated within `getGlobalTrackSelectionRun3ITSMatch::Run3ITSallAny`.

6.3   Track quality assurance

Track quality assurance is performed in this study involving a series of checks on different observables.

The following Subsections describe the main quality assurance criteria applied to the

data analyzed in this paper. The results presented here pertain to the
`LHC22_pass4_highIR_sampling` dataset.

An exception to this focus is the comparison of the transverse momentum spectra
between the high IR and low IR datasets, which is shown in Figure 15. From the analysis
of the ratio of the high IR p_T spectrum over the low IR p_T spectrum, it is possible to notice
a reduction in tracks within the high IR dataset. This discrepancy might be caused by the
diminished tracking efficiency in the high interaction rate environment. In fact, in such
environment, the density of collisions is higher, with potential overlap among particles.
Such conditions can complicate the track reconstruction process, impacting the tracking
efficiency and leading to fewer detected tracks in the high IR dataset compared to the
low IR dataset.

For additional results related to the `LHC22_pass4_lowIR` dataset, please refer to the
Appendix A.
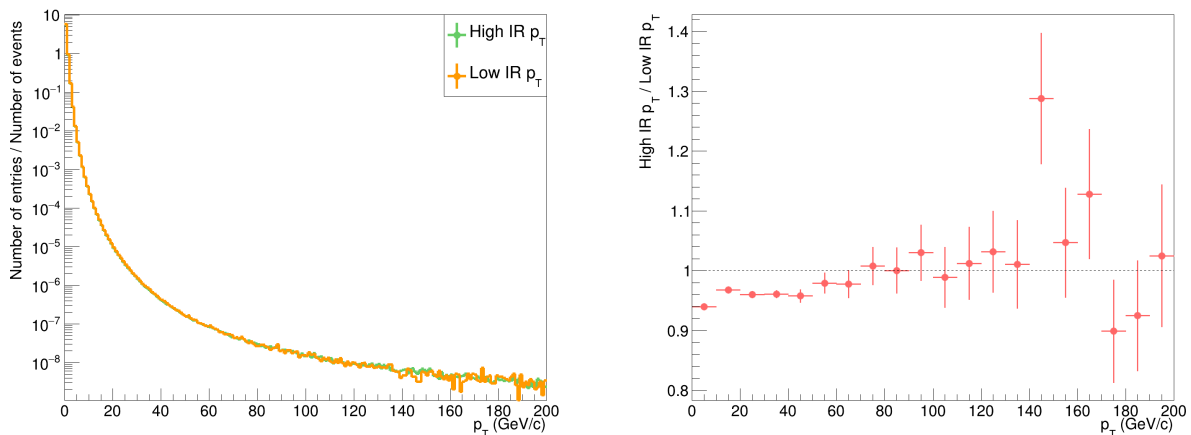
Figure 15: Left: comparison between the p_T spectrum of the high IR (green line) and low
IR (orange line) datasets. Right: ratio between the high IR p_T spectrum over the low IR
p_T spectrum.

6.3.1 Correlation of η and ϕ

The correlation of η and ϕ shows the 2-dimensional distribution of particle tracks in the
pseudorapidity (η) - azimuthal angle (ϕ) plane. These two observables are crucial in
describing the geometry of particle production and detection.
The correlation of η and ϕ histogram provides a representation of where particles are pro-
duced or detected in the detector and it can reveal patterns and asymmetries in particle
production and detection.

Figure 17 shows the correlation of η and ϕ across different momentum ranges for the
default GlobalTracks selection. These histograms reveal the presence of non-uniformities
in the η-ϕ distribution, which can be attributed to detector inefficiencies. The gaps, al-
ready visible at low p_T, become sharper when moving to higher p_T ranges: this is explained
by the fact that, at low p_T, tracks with lower momentum exhibit curved trajectories, en-
abling them to traverse the detector's gaps. Conversely, at high p_T, low-momentum
tracks are excluded, and the remaining tracks, which have high momentum and straight
trajectories, are less likely to intersect with the gaps.

6.3.2 Comparison of the momentum spectra for different cuts

To evaluate the impact of varying the cuts applied to track quality observables, Figure 18 provides a comparison of the p_T spectra for GlobalTracks selection, tight cuts, and loose cuts, as well as the ratios between tight cuts p_T spectrum over the GlobalTracks p_T spectrum and between loose cuts p_T spectrum over the GlobalTracks p_T spectrum. By examining the ratios of the p_T spectra, it is possible to notice that the tighter the cuts applied to the observables are, the more high-momentum tracks are excluded.

6.3.3 Resolution of the transverse momentum

The resolution of the transverse momentum $p_T\sigma(1/p_T)$ gives an idea of the spread in the measurements of the inverse transverse momentum of the particle. A low value of $p_T\sigma(1/p_T)$ means better resolution, and hence more precise measurements. Here, $\sigma(1/p_T)$ denotes the uncertainty associated with the inverse transverse momentum, derived from the covariance matrix of the track fitting process. This covariance matrix is crucial as it gives an estimation of the uncertainties and correlations of the fitted track parameters, thereby providing a comprehensive understanding of the precision involved in these measurements.

Figure 20 shows the transverse momentum resolution across the three different cut variations applied, requiring hits only in the inner ITS layers (top figure) and outer ITS layers (center figure), as well as requiring a TRD match for tracks (bottom figure).
In the scenario where hits in the inner ITS layers are required (Figure 20a), it is possible to observe five different populations of particles. However, when requiring hits only in the outer ITS layers (Figure 20b), the particle population at intermediate p_T disappears. This might be because particles associated with those tracks didn't interact with or weren't detected by the outer ITS layers. When requiring tracks with TRD match (Figure 20c), only one population remains. This is the population at lower uncertainty, so at better resolution. This observation, however, points to a limitation in the TRD's efficiency, as it appears to be sensitive to only one among the initially identified five particle populations.

6.3.4 Comparison of the overall momentum spectrum and the momentum spectrum for tracks with TRD match

To gain a deeper insight into the loss of TRD efficiency, Figure 19 shows the comparison between the comprehensive p_T spectrum against the p_T spectrum for tracks that have been successfully matched with the TRD. The comparison of the p_T spectra and the ratio of the p_T spectrum when tracks have TRD match over the overall p_T spectrum, reveals that the TRD accepts a maximum of approximately 22% of all tracks.
This loss of accepted tracks can be partially explained by the fact that not all the read-out chambers were installed. Specifically, the read-out pads in front of sectors 13, 14 and 15 (see Figure 16) were not installed in order to minimize the material in front of the PHOS detector [29]. This means that the TRD does not cover the whole radial space, consequently limiting the TRD's coverage across the entire radial span.
However, this factor alone doesn't fully account for the substantial 80% of tracks that go undetected by the TRD. This discrepancy may be due to inefficiencies within the TRD or the production of fake tracks by the ITS and TPC.
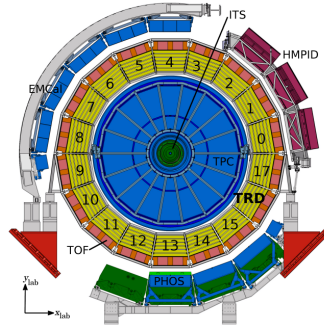
Figure 16: Schematic cross-section of the ALICE detector perpendicular to the LHC beam direction, showing the 18 sectors of the TRD, 3 of which (sectors 13-15) were not installed [29].

6.3.5 Findable and found TPC clusters

When a charged particle traverses the gas-filled chamber of the TPC, it ionizes the gas molecules producing electrons, which are drifted by an electric field to the chamber's readout system. The signal detected by the readout pads is called TPC cluster. In the radial direction there are 159 read-out pads, thus a particle flying away from the collision point in the radial direction can create a track with a maximum of 159 clusters.

Findable clusters are those clusters that should be detected by the TPC, so they represent the potentially detectable signal. Found clusters are the clusters that are actually detected by the readout system.

The number of findable and found TPC clusters are useful observables in track quality assurance because they give an indication of the tracking performance: a higher number of clusters associated with tracks indicates better tracking performance and more precise momentum and trajectory measurements. In addition, the comparison between findable and found clusters is crucial for evaluating the TPC performance: if a significant fraction of findable clusters is not found, it might indicate issues with the detector's operation or inefficiencies in the readout system.

High p_T tracks are expected to be associated with a greater number of TPC clusters since they carry more energy than low p_T tracks and so are able to transverse the whole radial direction of the TPC.

From Figure 21 it is possible to see that high p_T tracks are indeed associated with a high number of TPC clusters, but there is also a fraction of them which are associated with an intermediate value of TPC clusters. This is visible also from Figure 22, where two peaks appear in the projection of the number of found TPC clusters over the normalized number of events: one at the maximum number of TPC clusters, and another around 60 TPC clusters. Varying the cuts does not improve the situation in the high number of TPC clusters. However, when using tight cuts, the pick at intermediate number of TPC clusters disappears, leading to a better track reconstruction.

6.3.6 Number of crossed TPC rows

As the electrons produced by the ionization of the gas molecules travels through the TPC, they might cross over one of the concentric rows forming the readout pads. The number of crossed TPC rows for a given track is essentially a count of how many of these concentric rows the track has intersected.

The number of crossed TPC rows gives an indication of the track quality: a track with more crossed rows is typically more reliable because it is based on more data points.

From Figure 23, it appears that high p_T tracks exhibit fewer crossed rows. However, there are exceptions where high p_T tracks demonstrate expected behavior and cross the entire radial width of the TPC. In fact, the trajectory of particles with higher p_T tends to be straight, enabling them to span the full radial extent of the TPC under ideal conditions. The observed reduction in crossed rows for some high p_T tracks might therefore indicate that a portion of the track – either the beginning or the end – might be missing from the reconstruction. Cut variation does not enhance the observed frequency of high TPC crossed row counts.

6.3.7   Crossed TPC rows over findable clusters

The ratio of the number of crossed TPC rows over the number of findable clusters provides a measure of the track reconstruction efficiency. Ideally, a findable cluster is a pad row which based on the geometry of the track is a possible cluster [30], so a ratio equal to 1 indicates that the TPC is able to detect and record all the clusters as crossed rows. Values of this ratio greater than 1 might suggest issues in track reconstruction, like cluster merging, where multiple close-by clusters are counted as a single cluster. On the other hand, a ratio less than 1 can point to inefficiencies or issues in the ability of the TPC to detect and record all the clusters associated with a particle's trajectory.

Figure 24 displays a pick for this ratio around 1, which suggests that the TPC is performing efficiently, with minimal loss of information due to detector inefficiencies or cluster merging. In addition, tightening the selection criteria tends to exclude tracks with less reliable tracking information. As a result, tight cuts lead to a smaller likelihood of points below 1 than loose cuts, which instead allow more tracks with poor tracking conditions (e.g. passing through less sensitive areas of the TPC or affected by higher levels of noise) to be included.

6.3.8 χ^2 per TPC cluster

Once the clusters are detected, the expected position of the tracks can be calculated for each TPC pad row. The difference between the expected position and the measured one is measured by χ^2, which is normalized by the number of clusters.

A low value of χ^2 per number of clusters indicates a good quality fit for the tracks. On the contrary, a high value suggests discrepancies between the expected trajectory and the actual measurements, indicating a potential issue with the fit.

Figure 25 shows that high p_T tracks exhibit low values of χ^2 per TPC cluster, indicating high-quality track reconstruction. Tightening the selection criteria further enhances this quality, as evidenced by even lower χ^2 per TPC cluster values. Conversely, for low p_T tracks, employing looser cuts leads to a worse track reconstruction: specifically, the projection of the χ^2 per TPC cluster over the normalized number of events exhibits a plateau for high values of χ^2 per TPC cluster. To enhance reconstruction quality and eliminate this plateau, implementing tighter cuts proves to be more effective.

6.3.9   Number of ITS cluster

As in the TPC, when a charge particle traverses the ITS, it ionizes the detector material producing electrons that are collected by the ITS readout system and create signals called

clusters.

By analyzing the distribution of ITS clusters for tracks with different p_T values, one can assess how well the ITS performs in detecting and reconstructing tracks across various momentum ranges. A higher number of clusters associated with tracks indicates better tracking performance and more precise momentum and trajectory measurements.

Figure 26 shows that some of the high p_T tracks are associated to a surprisingly low quantity of ITS clusters. Given their elevated momentum, high p_T tracks are expected to traverse more ITS layers, leading to a higher number of clusters, compared to their low p_T counterparts. This deviation suggests a potential issue in track reconstruction. Tightening the cuts reduces the amount of high p_T tracks associated with low numbers of ITS clusters.

6.3.10   ITS hitmap

The ITS hitmap is a map of detected hits in the ITS. The hitmap allows to visualize where particles interact with the ITS and it provides insights into detector performance and efficiency. For instance, areas with a high density of hits indicate regions where many particles passed through and interacted with the ITS. Conversely, regions with no or few hits might suggest areas of inefficiency, potential issues, or simply regions that are less traversed by the particles in the given event sample.

Figure 27 reveals an unexpected trend: a significant portion of high p_T tracks is detected predominantly in the initial three layers of the ITS, despite the fact that their high energy and straight trajectories would facilitate traversal across the entire extent of the ITS. This observation implies issues in the track reconstruction process. Additionally, varying the selection criteria appears to yield minimal improvement.

6.3.11 χ^2 per ITS cluster

Like in TPC, the χ^2 per ITS cluster is a measurement of the difference between the expected position of the ITS clusters and the measured one. The smaller the value of χ^2 per number of clusters, the better the quality fit for the tracks. However, the χ^2 per ITS cluster reaches much higher values than the χ^2 per TPC cluster because the number of clusters over which χ^2 is normalized is greater in the TPC than in the ITS.

Figure 28 shows that a relevant fraction of high p_T tracks exhibit high values of χ^2 per ITS cluster, indicating potential issues with the quality fit. The variation of the selection criteria does not bring any improvement.
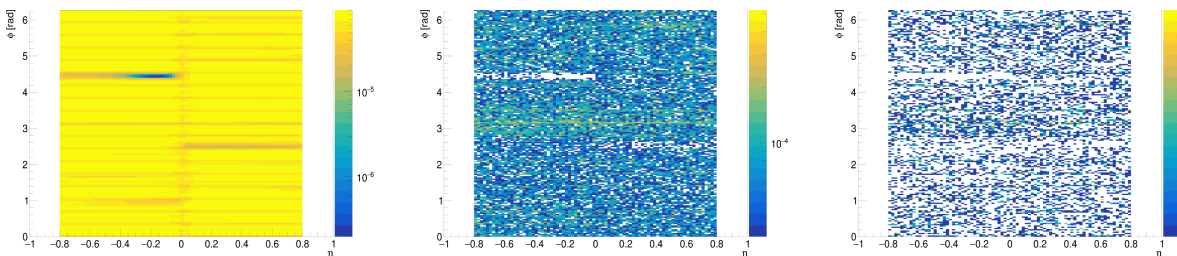
Figure 17: Correlation of η and ϕ with GlobalTracks selection for the following p_T ranges (from left to right): $3 < p_T < 5$ GeV, $50 < p_T < 100$ GeV, $100 < p_T < 200$ GeV.
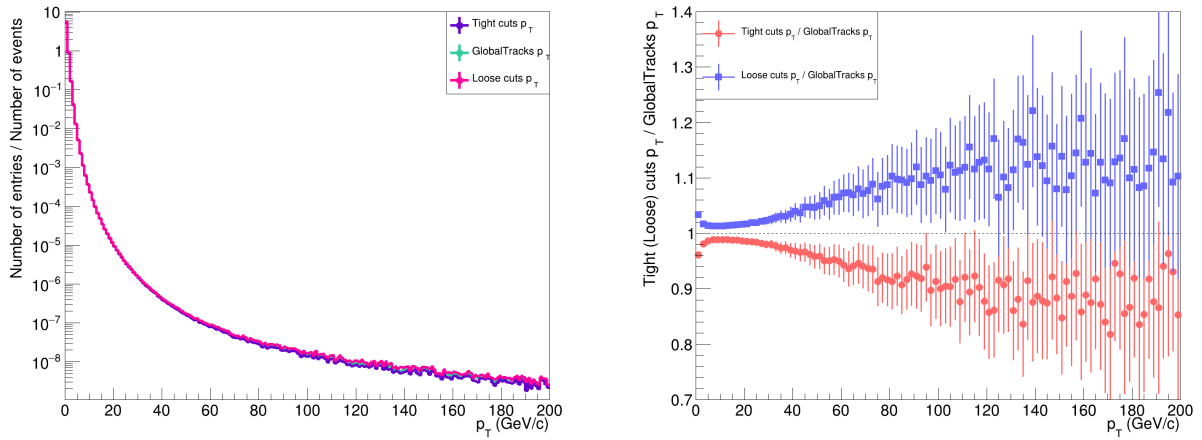
Figure 18: Left: comparison of the p_T spectra for GlobalTracks selection, tight cuts, and loose cuts. Right: ratios between tight cuts p_T spectrum over the GlobalTracks p_T spectrum (red) and between loose cuts p_T spectrum over the GlobalTracks p_T spectrum (blue).
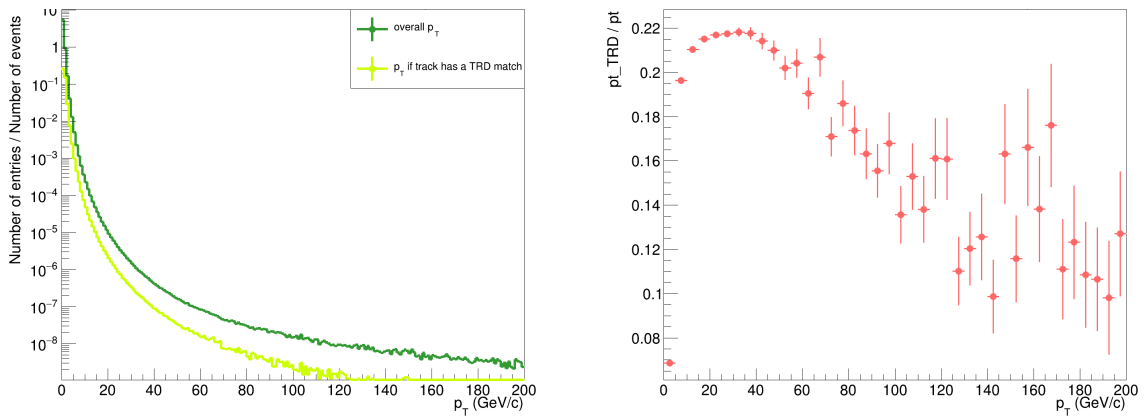
Figure 19: Left: comparison between the comprehensive $_T$ spectrum against the p_T spectrum for track with TRD match. Right: ratio of the p_T spectrum when tracks have TRD match over the overall p_T spectrum.
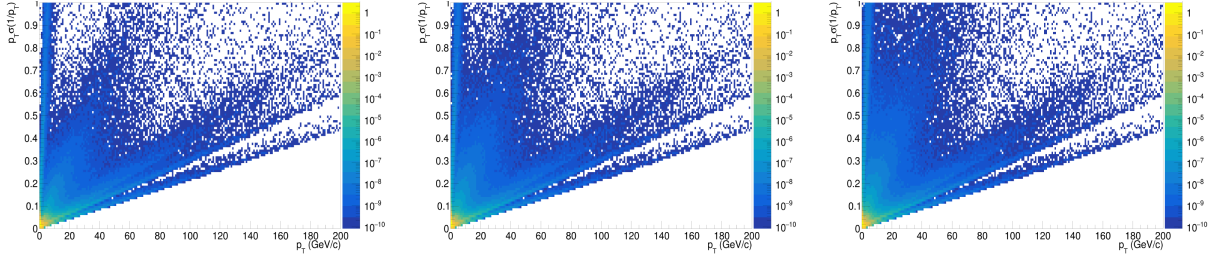
(a) Resolution of the transverse momentum when requiring hits in the 1st and 2nd ITS layers.
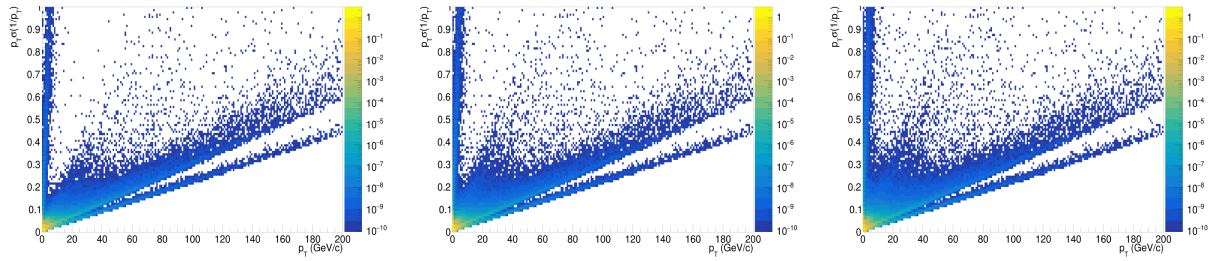
(b) Resolution of the transverse momentum when requiring hits in the 4th, 5th and 6th ITS layers.
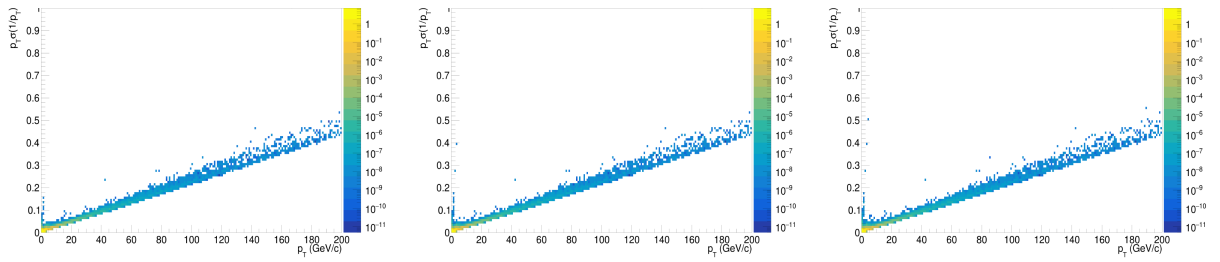
(c) Resolution of the transverse momentum when requiring tracks with TRD match.

Figure 20: Resolution of the transverse momentum for tight cuts, Global Tracks and loose cuts from left to right.
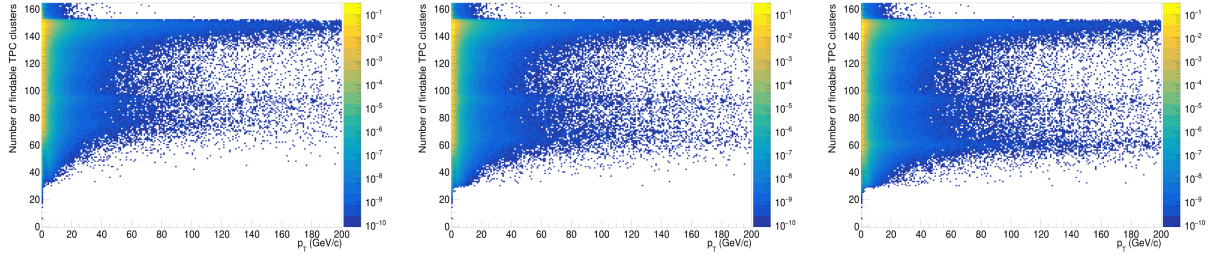
(a) Number of findable TPC clusters.
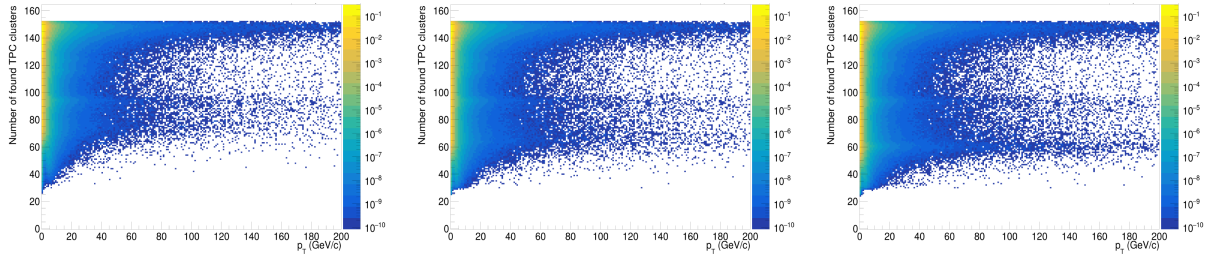
(b) Number of found TPC clusters.

Figure 21: Number of findable and found TPC clusters for tight cuts, Global Tracks and loose cuts from left to right.
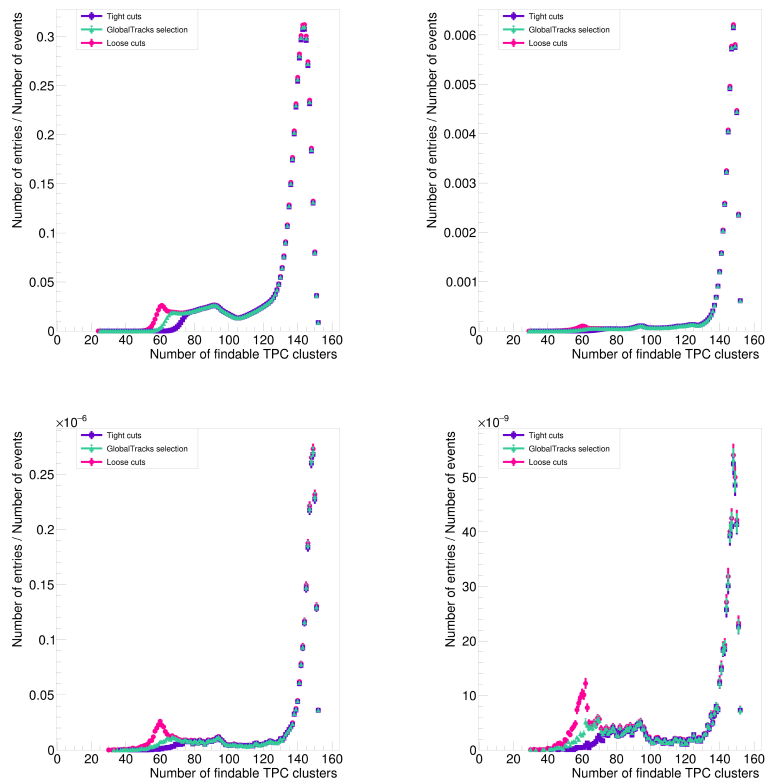
Figure 22: Projections of the number of found TPC clusters over the normalized number of events for four p_T ranges: $0 < p_T < 1$ GeV/c, $3 < p_T < 5$ GeV/c, $50 < p_T < 100$ GeV/c, $100 < p_T < 200$ GeV/c.
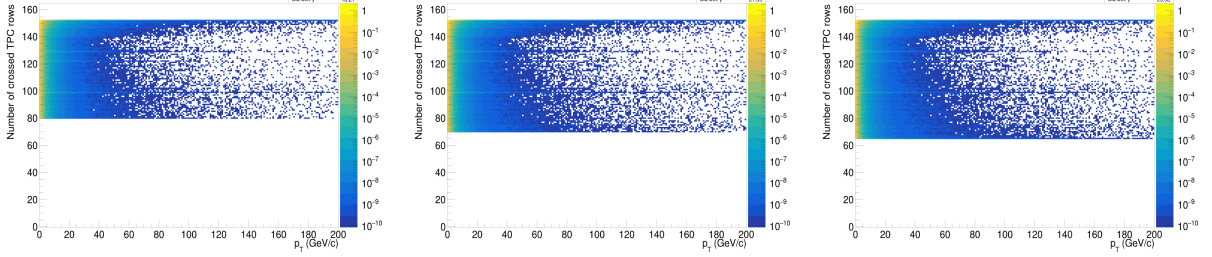
(a) Number of crossed TPC rows for tight cuts, Global Tracks and loose cuts from left to right.
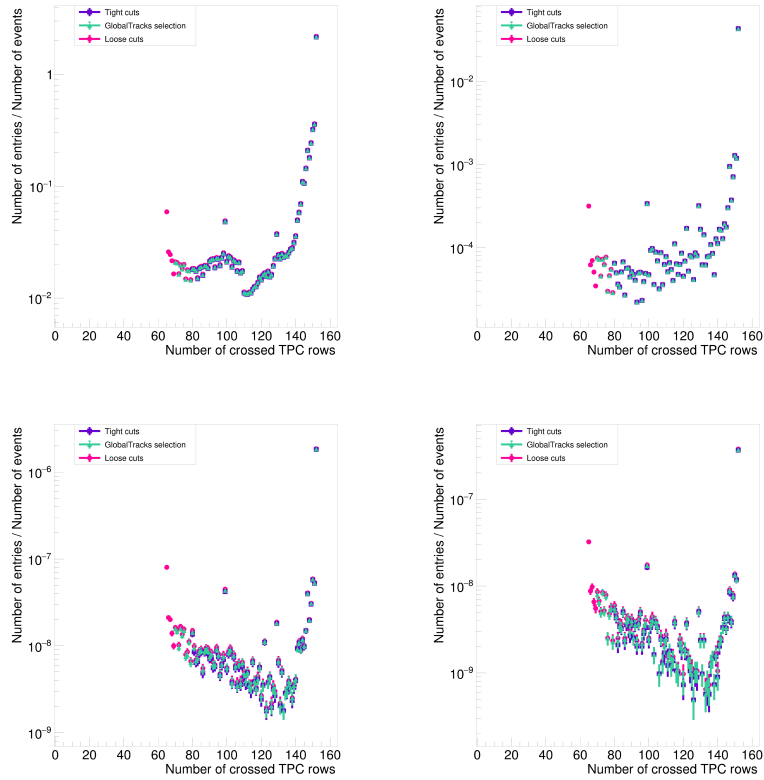
(b) Projections of the number of crossed TPC rows for four p_T ranges: $0 < p_T < 1$ GeV/c, $3 < p_T < 5$ GeV/c, $50 < p_T < 100$ GeV/c, $100 < p_T < 200$ GeV/c.

Figure 23
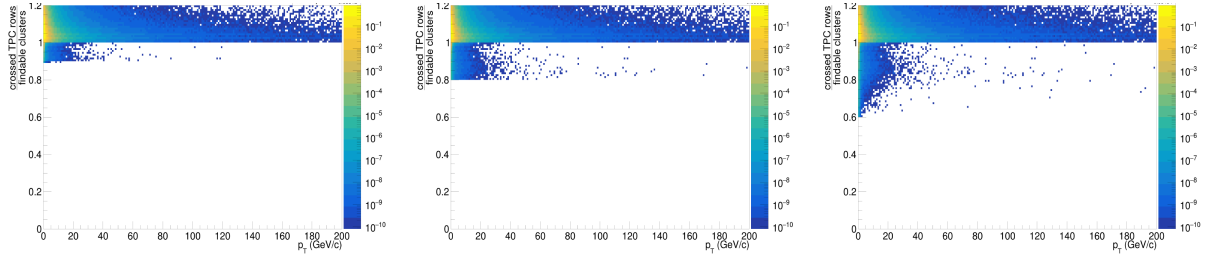
(a) Crossed TPC rows over findable clusters for tight cuts, Global Tracks and loose cuts from left to right.
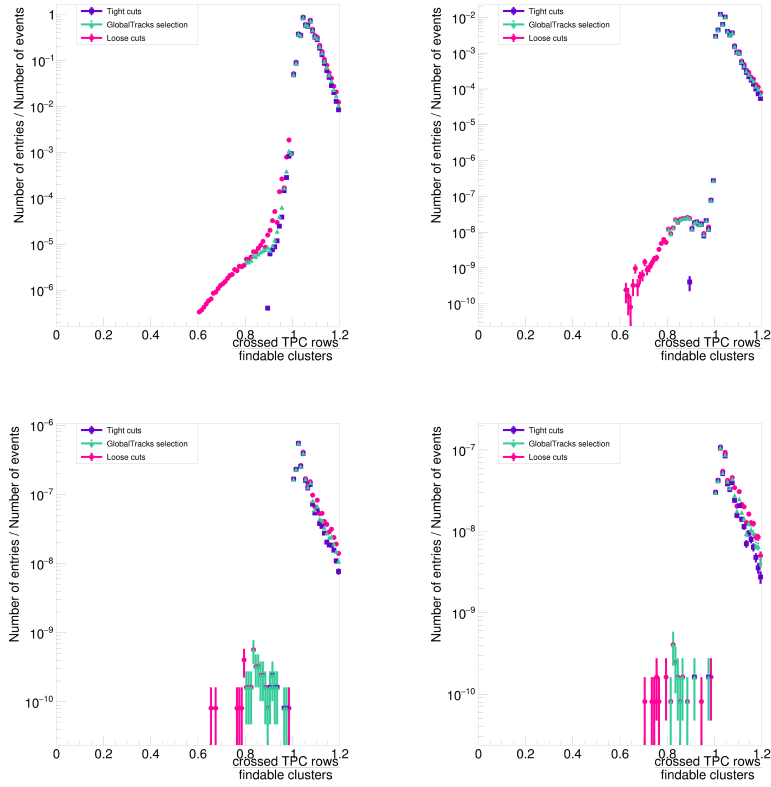
(b) Projections of crossed TPC rows over findable clusters for four p_T ranges: $0 < p_T < 1$ GeV/c, $3 < p_T < 5$ GeV/c, $50 < p_T < 100$ GeV/c, $100 < p_T < 200$ GeV/c.

Figure 24
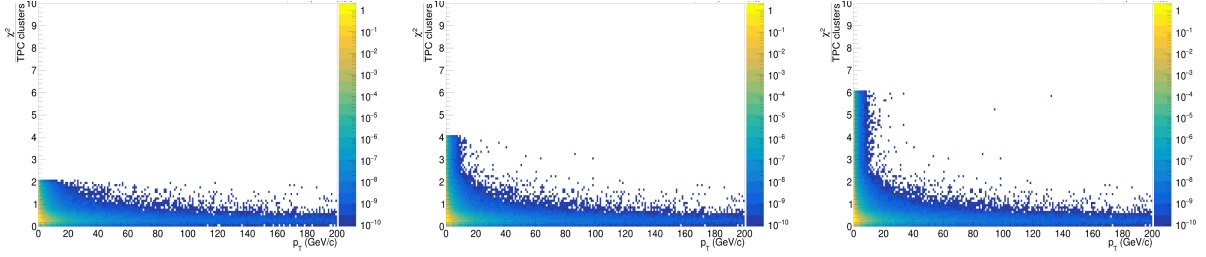
(a) χ^2 per TPC cluster for tight cuts, Global Tracks and loose cuts from left to right.
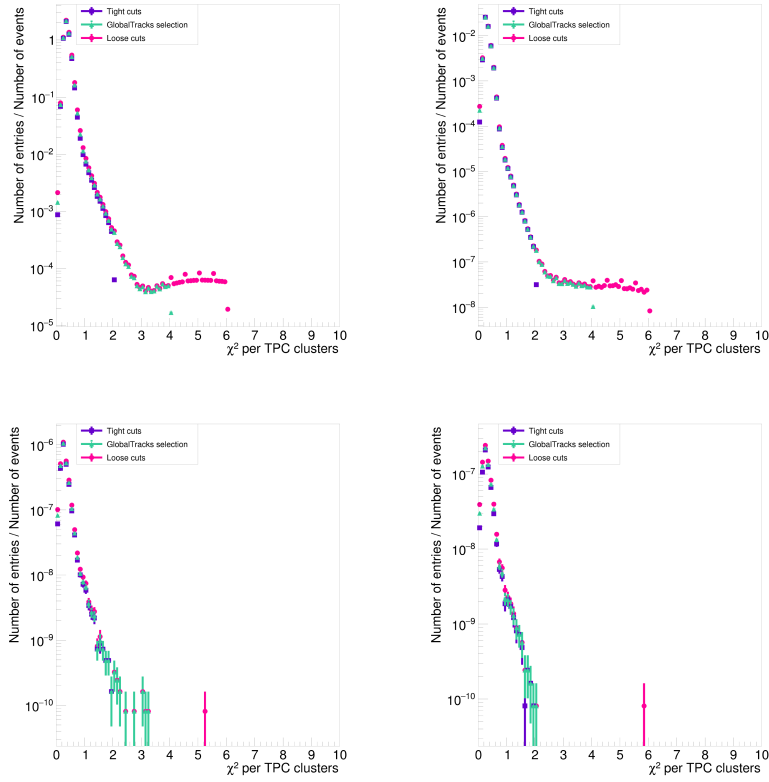
(b) Projections of χ^2 per TPC cluster for four p_T ranges: $0 < p_T < 1$ GeV/c, $3 < p_T < 5$ GeV/c, $50 < p_T < 100$ GeV/c, $100 < p_T < 200$ GeV/c.

Figure 25
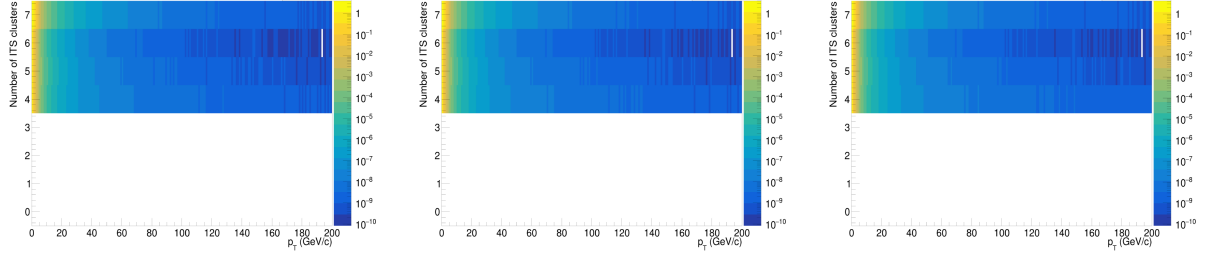
(a) Number of ITS clusters for tight cuts, Global Tracks and loose cuts from left to right.
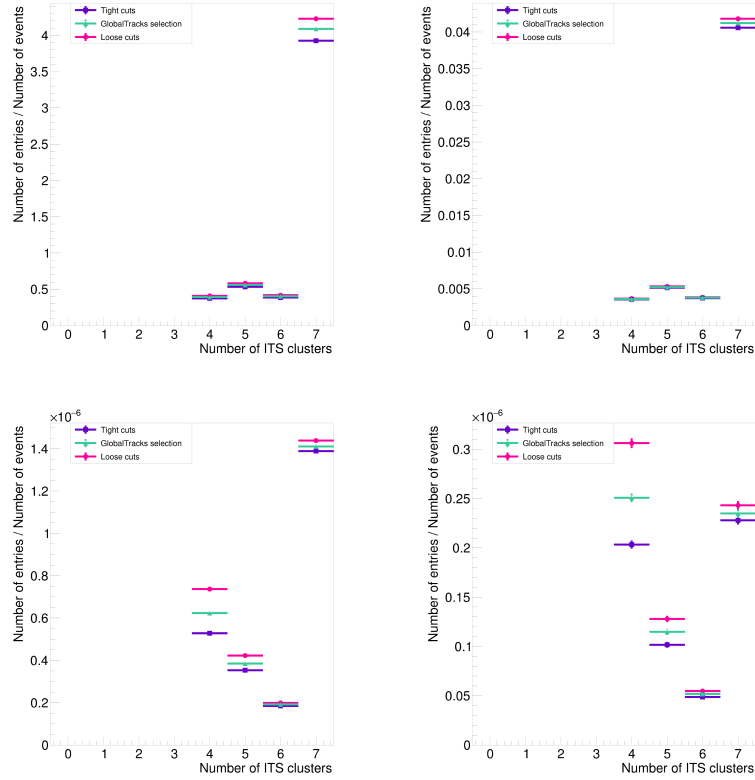
(b) Projections of the number of ITS clusters for four p_T ranges: $0 < p_T < 1$ GeV/c, $3 < p_T < 5$ GeV/c, $50 < p_T < 100$ GeV/c, $100 < p_T < 200$ GeV/c.

Figure 26
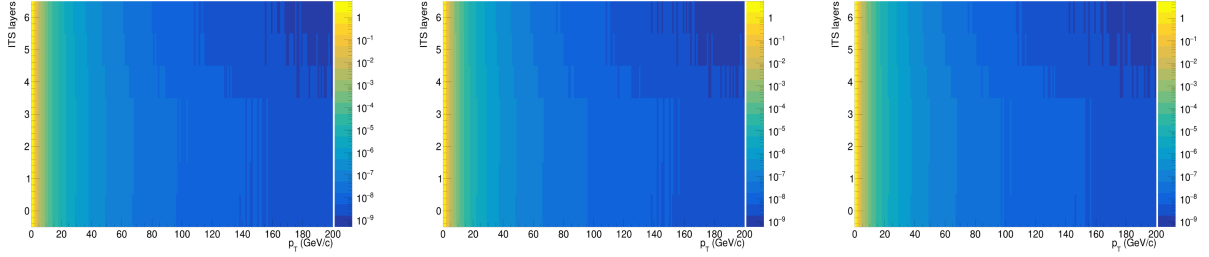
(a) ITS hitmap for tight cuts, Global Tracks and loose cuts from left to right.
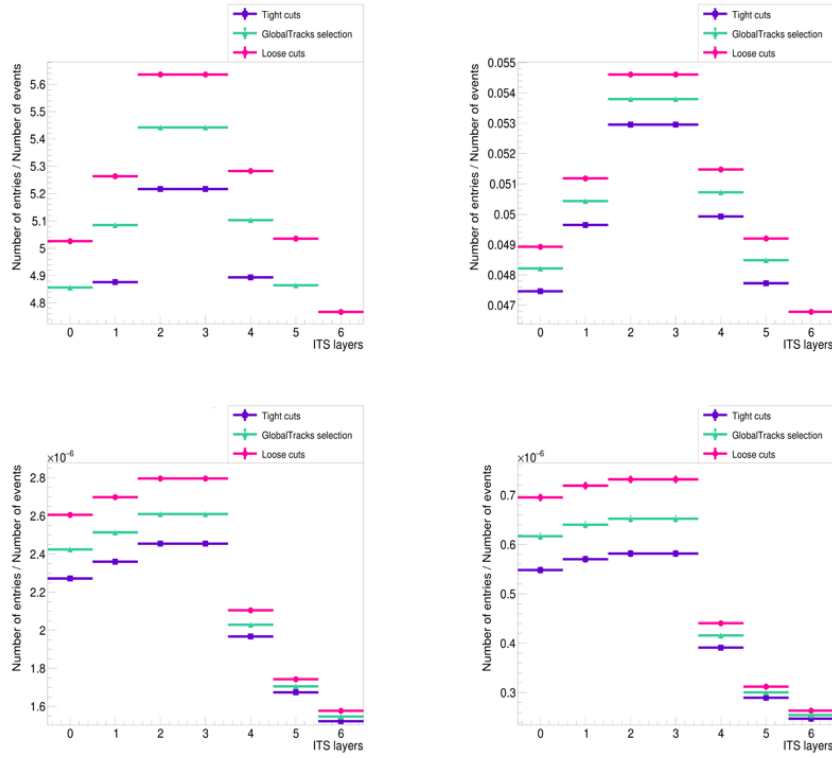
(b) Projections of the number of ITS layers for four p_T ranges: $0 < p_T < 1$ GeV/c, $3 < p_T < 5$ GeV/c, $50 < p_T < 100$ GeV/c, $100 < p_T < 200$ GeV/c.

Figure 27
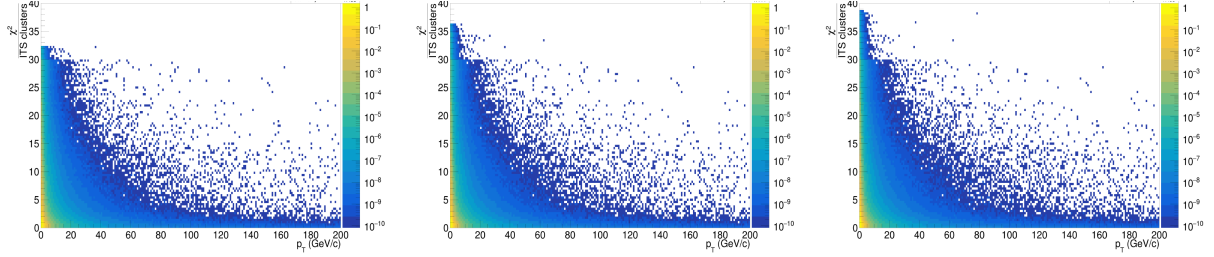
(a) χ^2 per ITS cluster for tight cuts, Global Tracks and loose cuts from left to right.
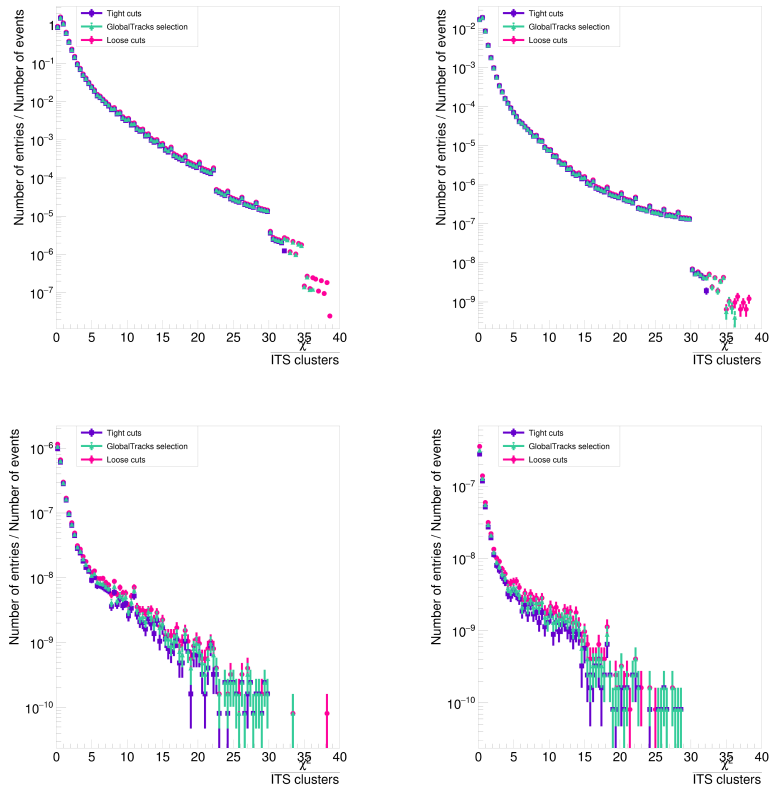
(b) Projections of χ^2 per ITS cluster for four p_T ranges: $0 < p_T < 1$ GeV/c, $3 < p_T < 5$ GeV/c, $50 < p_T < 100$ GeV/c, $100 < p_T < 200$ GeV/c.

Figure 28

6.4   Conclusions and outlook on track quality assurance

In this section, an extensive study on quality assurance was conducted on tracks of particles from proton-proton collision detected by the ALICE detector, with a focus on high p_T tracks. By adjusting the selection criteria across various track observables, the analysis unearthed a range of unexpected behaviors, caused by bad track reconstruction, inefficiencies in certain detector components, and production of fake high p_T tracks. Nevertheless, this analysis validated the expected behaviour for other track parameters, thereby assessing the quality of the analyzed data.

Future prospects on this analysis include applying this study also on Monte Carlo simulations, which will allow to further validate the results and to analyze the systematic uncertainties, and extending the cut variation study, with the aim of fine-tuning the selection criteria further and optimize the cuts on the tracks observables.

7 Results

Having assessed the quality of the data in the previous Section, this Section focuses on the study of the Primary Lund plane for charged jets from proton-proton collision recorded by the ALICE detector during the LHC Run3 in 2022. The datasets of interest are the same as those from the quality assurance analysis. Table 3 reports the LEGO trains used for this analysis.

The final aim of this study is to explore the behavior of the strong coupling constant as

Train run	Dataset
171056	`LHC22_pass4_highIR_sampling`
170683	`LHC22_pass4_lowIR`

Table 3: Train run and datasets

reflected by the variations in the Lund plane density, offering valuable insights into the underlying dynamics of QCD interactions.

The results presented here are derived from the `LHC22_pass4_highIR_sampling` dataset. For findings related to the `LHC22_pass4_lowIR` dataset, please refer to the Appendix B.

7.1 Primary Lund plane in (Δ, k_T)

Figure 29 shows the Primary Lund plane in the (Δ, k_T) plane for different p_T ranges. When analyzing the Primary Lund plane at high p_T intervals (Figure 29c), distinct regions with varying particle densities become apparent, as also illustrated in Figure 30. These variations in density are indicative of different physical processes contributing to the jet's internal structure.

The highest density region in the Lund plane, at low energies and large angles (low $\ln(k_T/\text{GeV})$ and low $\ln(\Delta/R)$), is due to soft emissions, including those from Initial State Radiation (ISR) and Multi-Parton Interactions (MPI/UE), as well as detector effects. ISR is the radiation of gluons emitted by the incoming partons as they approach each other before the hard scattering event occurs. This radiation contributes to the particle multiplicity in the event, particularly at low energies. MPI refers to the soft scatterings between partons not participating in the primary interaction, which lead to a further increase of the density of soft particles. These phenomena, combined with the QCD infrared safety property where the probability for gluons to emit other gluons at low energies is higher than at high energies, contribute to the increase of density in this region of the Lund plane.
In addition, at large angles and low energy, the tracking efficiency of the detector worsens because trajectories of soft particles are harder to reconstruct accurately.
To correct for detector effects, a 3D unfolding procedure is essential. This process has been already implemented by the ALICE Collaboration in a previous study [17] and involves matching jets and their internal splittings between simulated (generator level) and observed (detector level) data based on specific geometric criteria, allowing for a more accurate representation of the underlying physics phenomena.

The region below $\ln(k_T/\text{GeV})$=0 in the Primary Lund plane is particularly interesting because the running of the strong coupling constant becomes visible. In fact, as the
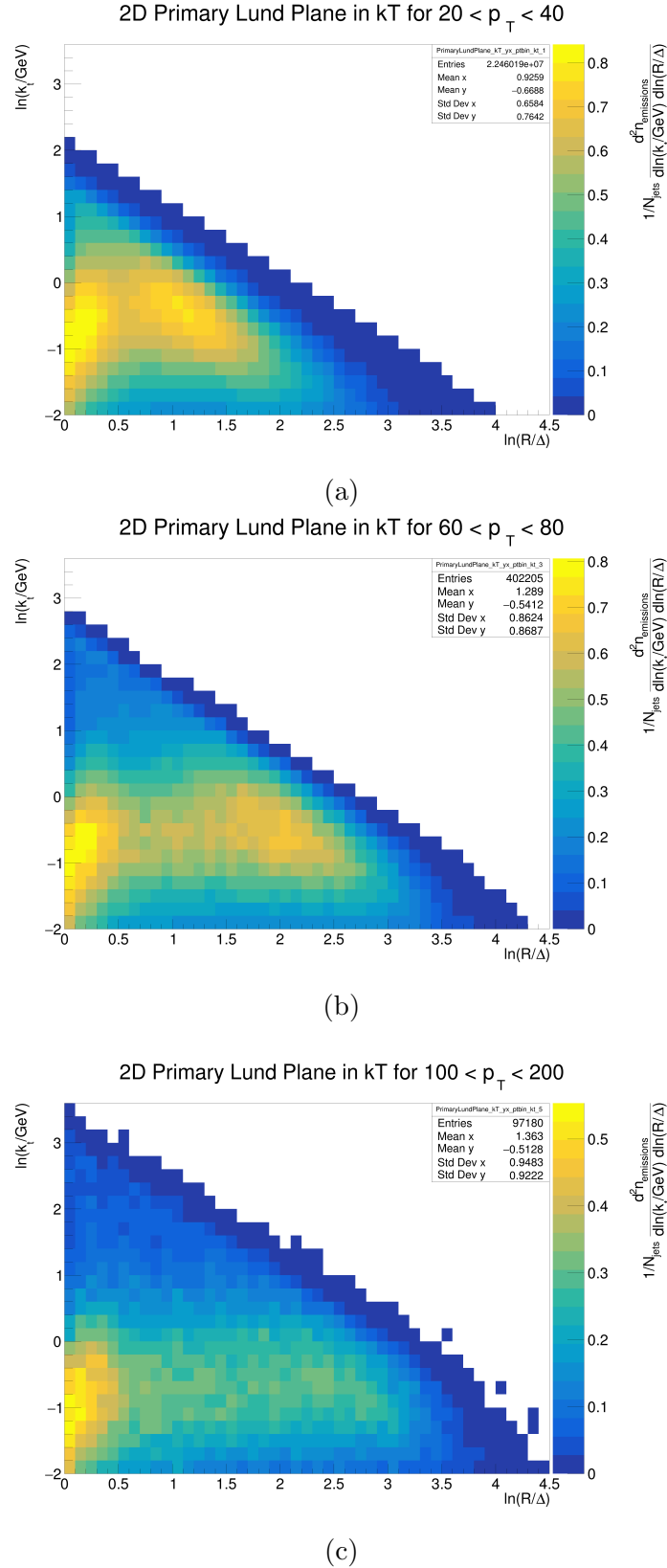
Figure 29: Primary Lund plane in (Δ, k_T) for different momentum ranges.

energy scale decreases, the strong coupling constant increases (see Equation 1). Since the average Lund plane density is directly proportional to the strong coupling constant (see
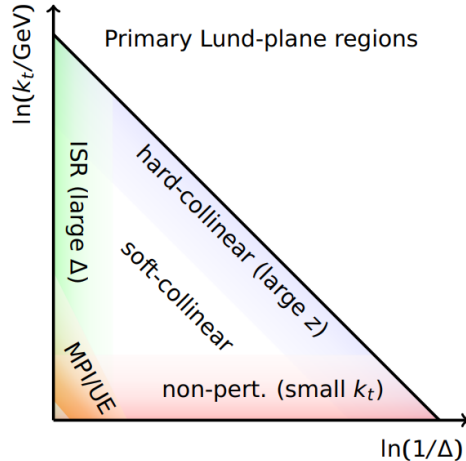
Figure 30: Schematic representation of the different regions of the Lund plane [13].

Equation 9), an increase in the strong coupling constant leads to a higher density region in the Primary Lund plane.

Moreover, this region marks the transition from the perturbative region, where α_s is still small and perturbative calculations are still valid, to the non-perturbative region, where α_s is so big that perturbative calculations break.

In the non-perturbative region, at very low $\ln(k_T/\text{GeV})$ values, the density decreases due to non-perturbative effects, like hadronization and confinement of quarks and gluons into hadrons, which cause a decrement of the density in the Lund plane.

Due to angular ordering and momentum conservation of the jet formation process, the Lund plane density cannot exceed the diagonal line given by $k_T < \frac{1}{2}p_{T,\text{jet}}\Delta$, which represents the kinematic limit of the Lund plane. Nevertheless, due to the degradation of the harder branch during the jet declustering sequence, smearings above the kinematic limit may appear.

The region right below the kinematic limit, where z is large, is characterized by a low Lund plane density, caused by the energy loss of the leading branch due to hard-collinear effects. In fact, during the evolution of the jet, a parton can split into two or more partons. If the offspring partons carry a big fraction of the parent parton's momentum, the splitting is called hard. In addition, if the offspring partons are emitted at small angles relative to the direction of the parent parton, the splitting is called collinear. Thus, since the parent partons lose a fraction of their energy due to hard-collinear branchings, the energy available for subsequent emissions is reduced, and this is reflected in a reduction of the Lund plane density in this region.

A comparative analysis of the Primary Lund plane obtained in this study with the one from the ALICE Collaboration for pp collisions at 13 TeV during Run2 of LHC [17], is insightful. Figure 31 presents the Primary Lund plane obtained by the ALICE Collaboration in 2021 for charged-particle jets in the transverse momentum range of $20 < p_T < 120$ GeV/c. Upon comparing this with Figure 29c, it is possible to observe remarkable similarities in their structures and density distributions. However, it's important to point out that the Primary Lund plane in Figure 31 has been corrected for detector effects through an unfolding procedure.

It is convenient to also examine slices of the Lund plane density in specific ranges of $\ln(R/\Delta)$ and $\ln(k_T/\text{GeV})$.
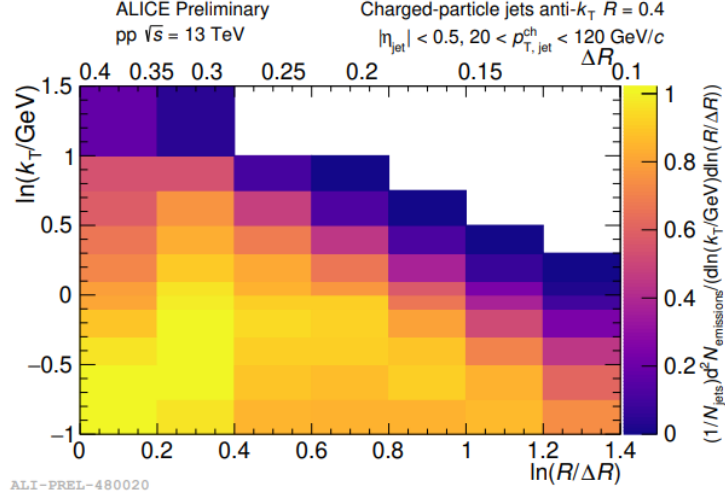
Figure 31: Fully corrected primary Lund plane density obtained by the ALICE Collaboration in 2021 for charged-particle jets in the transverse momentum range of $20 < p_T < 120$ GeV/c [17].

The left panel of Figure 32 shows slices of the high p_T primary Lund plane in the wide splitting regions - so for low $\ln(R/\Delta)$ values - (figure above) and in the narrow splitting regions - so for high $\ln(R/\Delta)$ values - (figure below). The right panel, instead, shows the projections of the primary Lund plane density in the wide and narrow splitting regions obtained by the ALICE Collaboration in [17], which compare four different MC models: PYTHIA8 Monash [31], Sherpa 2.2.8 [32], and Herwig 7 [33].

The comparison reveals a consistent agreement between the projections obtained in this study and in [17] both in the wide and narrow splitting regions. From both sets of results, the running of the strong coupling constant is evident: at lower energy scales, the increase in the strong coupling constant leads to a higher density, while at higher energy scales, the density diminishes as the strong coupling constant decreases. Moreover, these projections delineate the transition from non-perturbative to perturbative regimes.

The same comparison can be performed for slices of the primary Lund plane in the perturbative (large $\ln(k_T/\mathrm{GeV})$) and non-perturbative (small $\ln(k_T/\mathrm{GeV})$) regions. Figure 33 shows the projection of the primary Lund plane density obtained in this study and in [17] for slices of $\ln(k_T/\mathrm{GeV})$. This comparison highlights notable discrepancies in the trends of the projections between this study and the findings reported by [17], both in the non-perturbative and in the perturbative region. These divergences can be attributed to the absence of detector effect corrections in the results obtained in this study. Thus, once the correction scheme is implemented, it is expected that the results will align more closely.
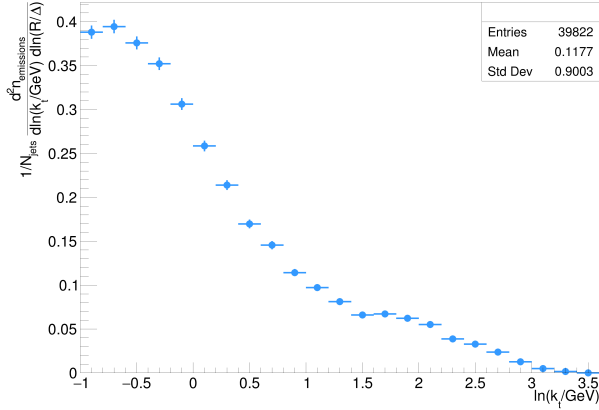
(a) Projection of the primary Lund plane density in the $100 < p_T < 200$ GeV/c range over the $\ln(k_T/\text{GeV})$ axis in the wide splitting region ($0 < \ln(R/\Delta) < 1$).
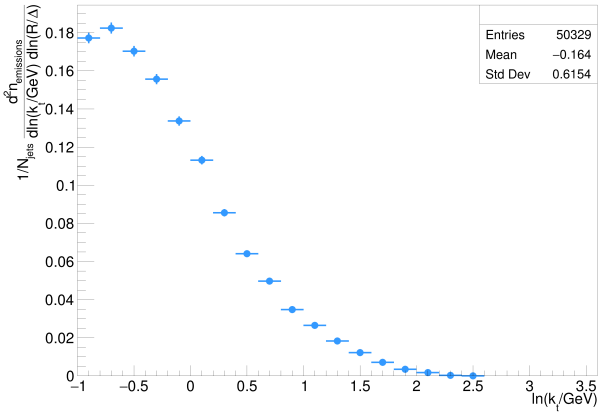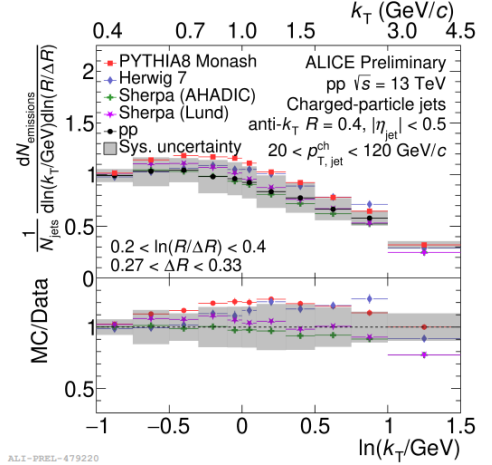
(b) Projection of the primary Lund plane density over the $\ln(k_T/\text{GeV})$ axis in the wide splitting region ($0.2 < \ln(R/\Delta) < 0.4$) calculated by [17].
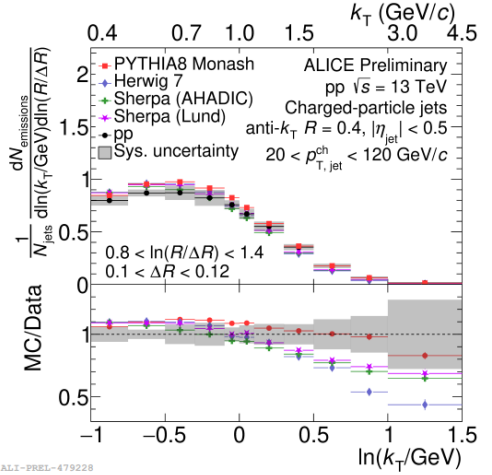
(c) Projection of the primary Lund plane density in the $100 < p_T < 200$ GeV/c range over the $\ln(k_T/\text{GeV})$ axis in the narrow splitting region ($1 < \ln(R/\Delta) < 4.5$).

(d) Projection of the primary Lund plane density over the $\ln(k_T/\text{GeV})$ axis in the narrow splitting region ($0.8 < \ln(R/\Delta) < 1.4$) calculated by [17].

Figure 32
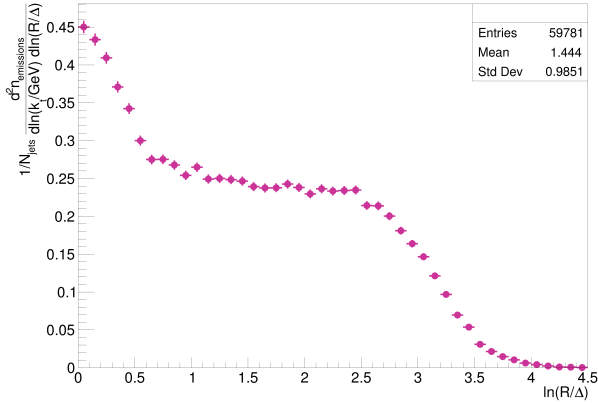
(a) Projection of the primary Lund plane density in the $100 < p_T < 200$ GeV/c range over the $\ln(R/\Delta)$ axis in the non-perturbative region $(-2 < \ln(k_T/\text{GeV}) < 0)$.
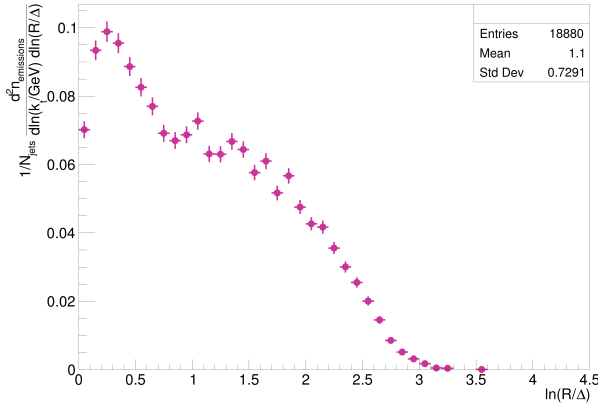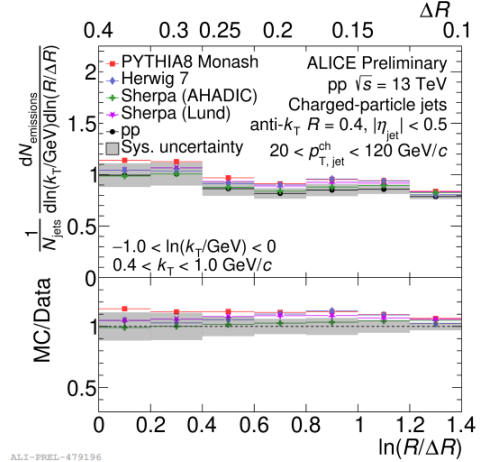
(b) Projection of the primary Lund plane density over the $\ln(R/\Delta)$ axis in the non-perturbative region $(-1 < \ln(k_T/\text{GeV}) < 0)$ calculated by [17].
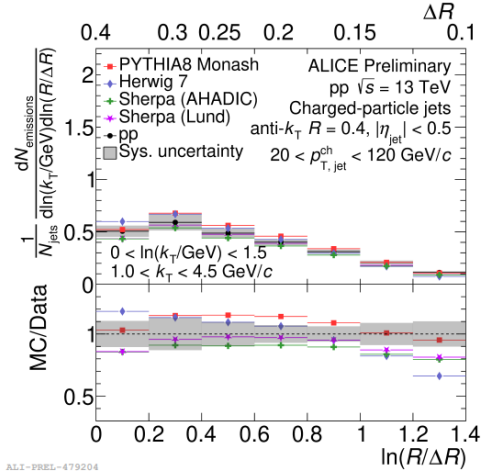
(c) Projection of the primary Lund plane density in the $100 < p_T < 200$ GeV/c range over the $\ln(R/\Delta)$ axis in the perturbative region $(0 < \ln(k_T/\text{GeV}) < 3.5)$.

(d) Projection of the primary Lund plane density over the $\ln(R/\Delta)$ axis in the perturbative region $(0 < \ln(k_T/\text{GeV}) < 1.5)$ calculated by [17].

Figure 33

7.2 Primary Lund plane in (Δ, z)

The Primary Lund plane can be expressed also in terms of the observable z instead of k_T. Figure 34 shows the Primary Lund plane in the (Δ, z) plane for different p_T ranges.

Focusing on the Primary Lund plane at high p_T intervals (Figuree 34c), different density regions can be identified like in the case of the Primary Lund plane in (Δ, k_T), as also illustrated in Figure 35.

The region at highest density in the plane, at large angles and low energies (so at large $\ln(R/\Delta)$ and large $\ln(1/z)$), accounts for soft emission, including ISR and MPI, and detector effect. The latter contribution to the density needs to be corrected via unfolding, which has been implemented in the Lund jet plane obtained by the ATLAS collaboration [16].

The area around the diagonal line at $k_T = \Lambda_{QCD}$ is another high density region in the Primary Lund plane due to the increase of the strong coupling constant at low energy. This region if of great interest not only because the running of the strong coupling constant is visible, but also because this line marks the transition from the perturbative ($k_T > \Lambda_{QCD}$) to the non-perturbative ($k_T < \Lambda_{QCD}$) regime.

Emissions that fall in the non-perturbative region are suppressed due to non-perturbative effects, causing a decrease of the Primary Lund plane density.

There is a suppression of emissions also in the perturbative region at small angles and large energies due to hard-collinear effects, which cause a loss of energy of the leading branch.

It is useful to compare the Primary Lund plane in (Δ, z) obtained in this study with the one measured by the ATLAS Collaboration in 2020 for pp collision at 13 TeV from Run2 using jets at $p_T > 675$ GeV/c [16]. Figure 36 shows the Primary Lund plane obtained by the ATLAS Collaboration. The comparison with Figures 34c reveals similarities in the density distribution, despite the jets used in [16] have a way higher p_T than those used for this analysis. Additionally, it's important to consider the ATLAS Primary Lund plane has been unfolded to take care of the detector effects.

Figures 37 and 38 show the comparison of the Primary Lund plane density projected respectively over the $\ln(R/\Delta)$ and $\ln(1/z)$ axes for different ranges obtained in this study (left panel) and in [16] (right panel), which compare different MC generators (Pytha, Sherpa, and Herwig).

It is possible to see that the results obtained by this study agree with those obtained by [16].

Specifically, Figures 38a and 38b highlight the ability of the Primary Lund plane to isolate effect arising from parton shower to hadronization models as the emissions change from wide-angles to collinear. In fact, for small angles (so large $\ln(R/\Delta)$), there is an enhancement of the density due to collinear emissions associated with parton shower effects. Conversely, at large angles (so small $\ln(R/\Delta)$), the region is populated by wide-angles emissions associated with hadronization effects.

Figures 37a and 37b illustrate an increase of the density when moving to low energy scales (so large $\ln(1/z)$) due to soft-emission effects.

The decrease of density visible in Figures 37c and 37d and Figures 38c and 38d is due to non-perturbative effects, as these figures show projections of the Primary Lund plane in the non-perturbative region.
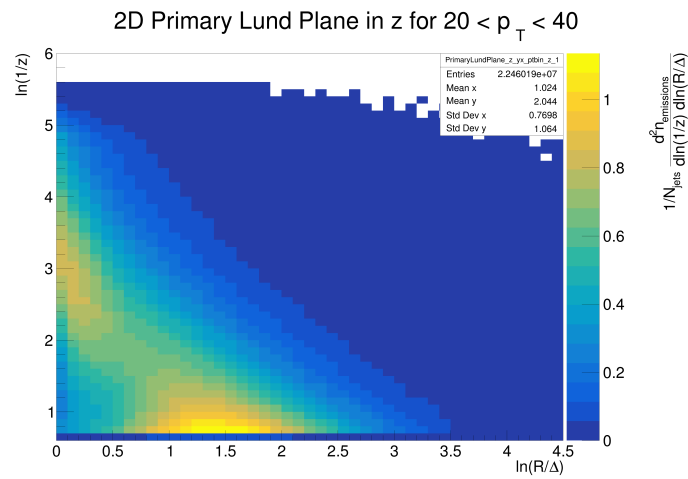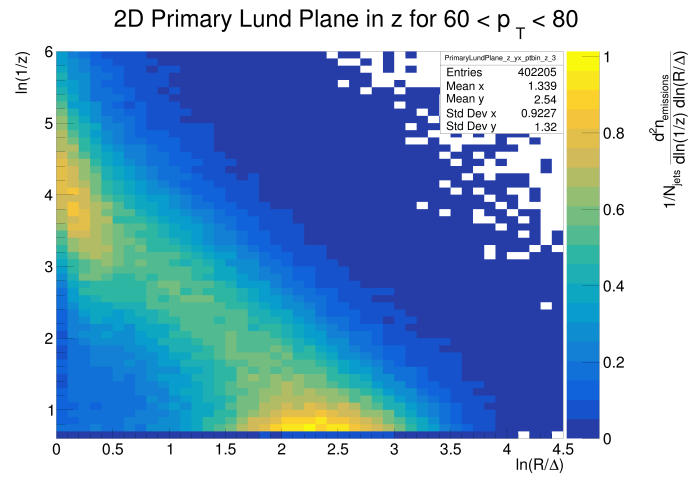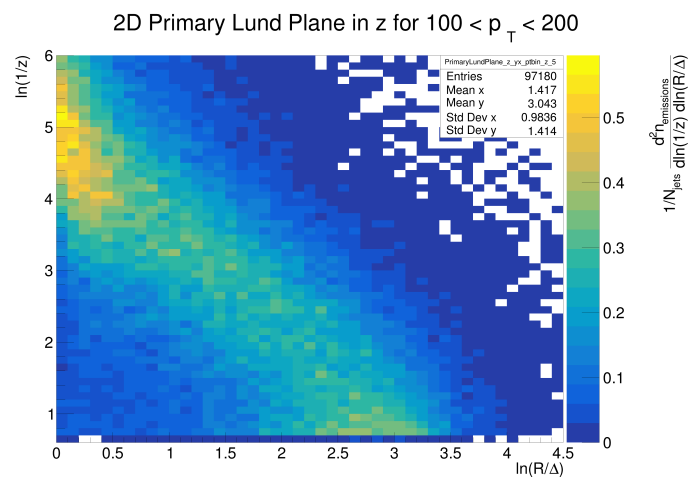
Figure 34: Primary Lund plane in the (Δ, z) plane for different momentum ranges.
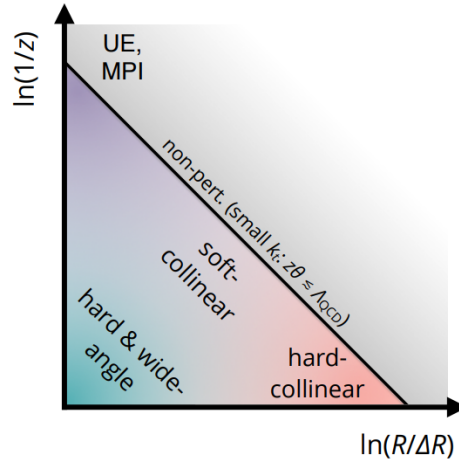
Figure 35: Schematic representation of the different regions of the Lund plane [16]
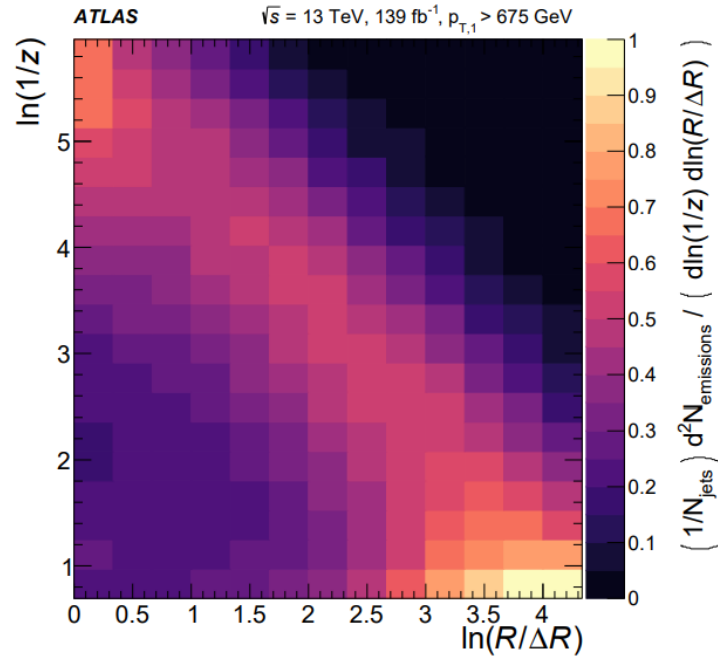
Figure 36: Corrected Primary Lund plane density obtained by the ATLAS Collaboration in 2020 for jets at $p_T > 675$ GeV/c [16].
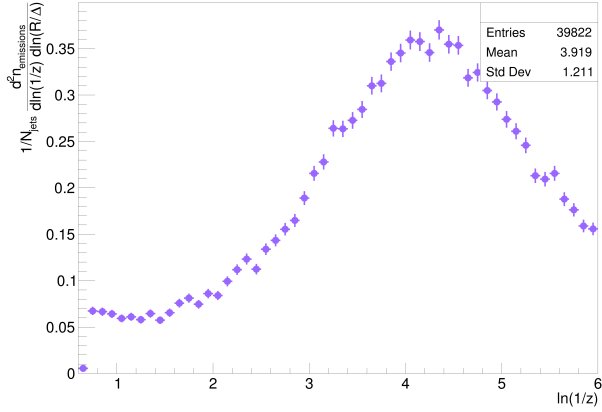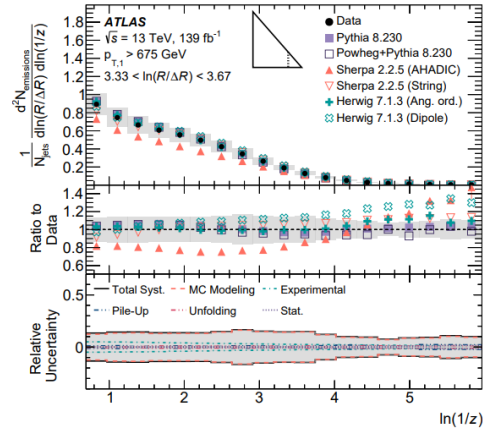
(a) Projection of the primary Lund plane density in the $100 < p_T < 200$ GeV/c range over the $\ln(1/z)$ axis in the wide splitting region ($0 < \ln(R/\Delta) < 1$).
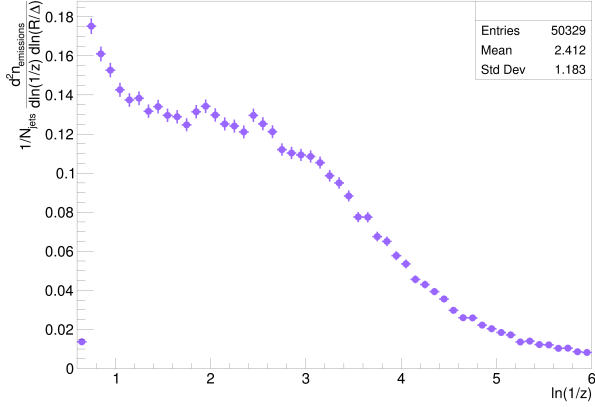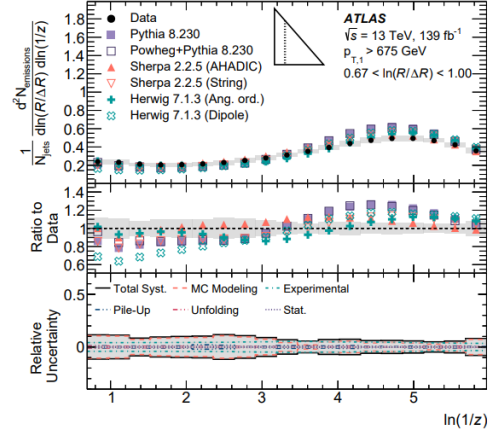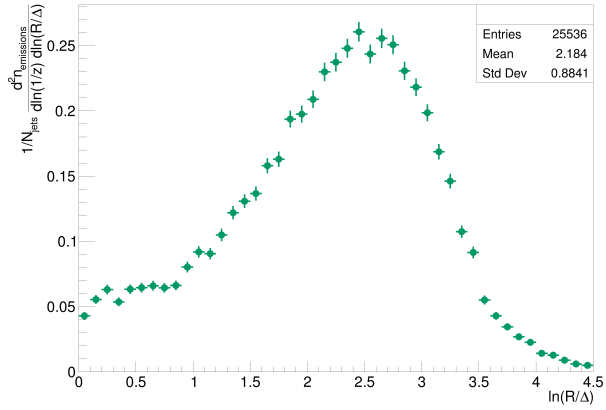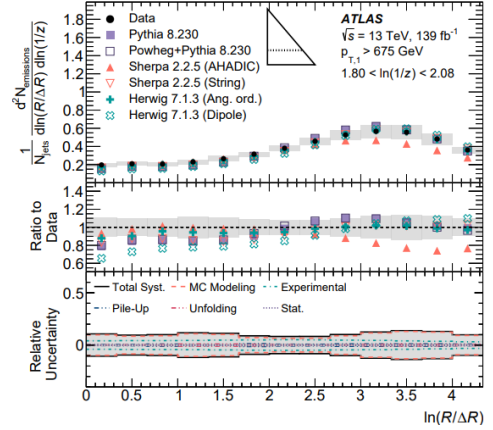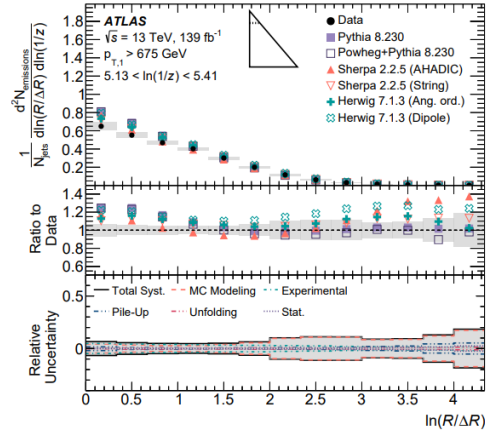

(b) Projection of the primary Lund plane density over the $\ln(1/z)$ axis in the wide splitting region ($0.67 < \ln(R/\Delta) < 1$) calculated by [16].

(c) Projection of the primary Lund plane density in the $100 < p_T < 200$ GeV/c range over the $\ln(1/z)$ axis in the narrow splitting region ($1 < \ln(R/\Delta) < 4.5$).

(d) Projection of the primary Lund plane density over the $\ln(1/z)$ axis in the narrow splitting region ($3.33 < \ln(R/\Delta) < 3.67$) calculated by [16].

Figure 37

(a) Projection of the primary Lund plane density in the $100 < p_T < 200$ GeV/c range over the $\ln(R/\Delta)$ axis in the non-perturbative region $(0.6 < \ln(1/z) < 2)$.
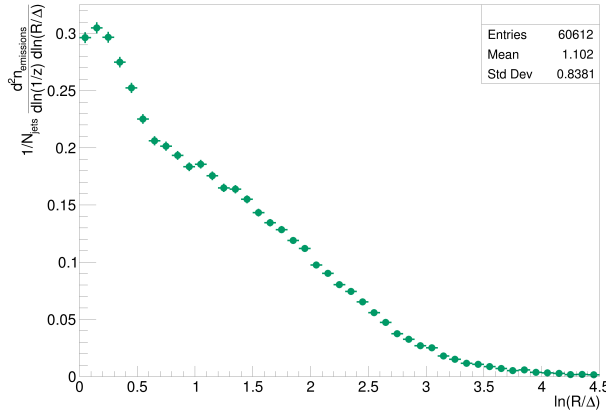
(b) Projection of the primary Lund plane density over the $\ln(R/\Delta)$ axis in the non-perturbative region $(1.8 < \ln(1/z) < 2.08)$ calculated by [16].

(c) Projection of the primary Lund plane density in the $100 < p_T < 200$ GeV/c range over the $\ln(R/\Delta)$ axis in the perturbative region $(2 < \ln(1/z) < 6)$.

(d) Projection of the primary Lund plane density over the $\ln(R/\Delta)$ axis in the perturbative region $(5.13 < \ln(1/z) < 5.41)$ calculated by [16].

Figure 38

7.3   Conclusion and outlook on the Primary Lund plane results

In conclusion, the analysis of the Primary Lund plane for charged jets from proton-proton collisions at $\sqrt{s}$ =13.6 TeV during Run 3 detected by the ALICE detector provided in this Section presents several key observations.

First of all, it shows that the Primary Lund plane can be experimentally used as a tool not only for representing the jet's internal structure but also for probing the interactions among the jet's constituents.

In addition, it proves that from the study of the Primary Lund plane density one can observe the running of the strong coupling constant and the effects of other physics phenomena, like soft emissions and hard-collinear effects.

Furthermore, the agreement between the results obtained in this study and those obtained from other experimental studies attests to the robustness and reliability of the current analysis.

Looking forward, the introduction of a correction scheme is imperative to take into account the detector effects contributing to the Primary Lund plane density.

Additionally, to further validate the experimental results the analysis has to be extended to Monte Carlo simulations.

Finally, an investigation into the systematic uncertainty associated with the measurements needs to be performed.

8   Conclusion

This thesis provides the first measurement of the Primary Lund plane for charged jets from proton-proton collision at $\sqrt{s} =$13.6 TeV collected in Run 3 with the ALICE detector.

The primary Lund plane is a theoretical representation of the phase space of jet emissions, which are reconstructed using the anti-k_T algorithm, and reclustered using the Cambridge-Aachem algorithm. The different stages of the fragmentation process are represented as points in the Primary Lund plane, which is constructed using a declustering sequence that collects the jet's information step by step.

From the analysis of the Primary Lund plane density, both in the (Δ, k_T) and (Δ, z) planes, it is possible to observe different regions to which different physics phenomena contribute: the running of the strong coupling constant, the soft emissions and the hard-collinear branchings, together with non-perturbative effects.

The effects of the different contributions to the Primary Lund plane density become pronounced when projecting the Primary Lund plane density onto specific regions of the phase space.

The results obtained in this analysis are compared with other experimental results, highlighting the Lund plane's utility as a robust tool for extracting information on the interactions occurring in jet emissions and, specifically, on the strong force.

This study lays a foundational framework for further analysis of the Primary Lund plane, offering a methical approach for declustering jets and representing their substructures within the Primary Lund plane.

Moreover, this thesis provides a detailed study of the quality and reliability of the data of two collections of Run 3 datasets within the ALICE experiment, identifying unexpected behaviors of some track observables and providing methodologies for fine-tuning the track's parameters. In addition, the study serves as a benchmark for future investigations on track quality assurance for both proton-proton and lead-lead collisions.

A   Appendix

This Appendix shows the results obtained by performing track quality assurance on the `LHC22_pass4_lowIR` dataset.
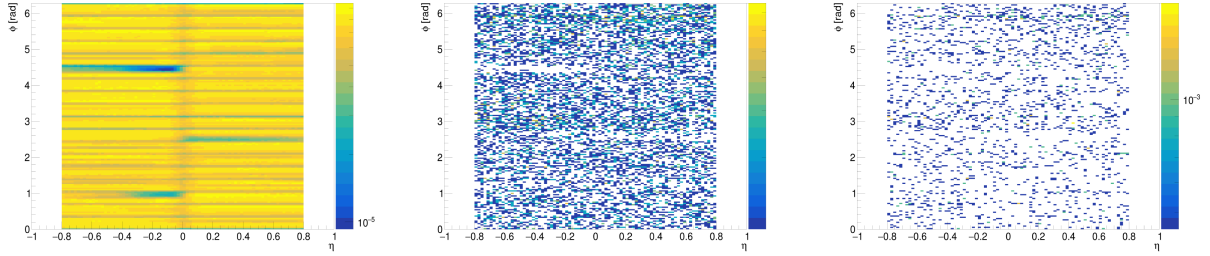
Figure 39: Correlation of η and ϕ for GlobalTracks selection for the following p_T ranges (from left to right): $3 < p_T < 5$ GeV, $50 < p_T < 100$ GeV, $100 < p_T < 200$ GeV.
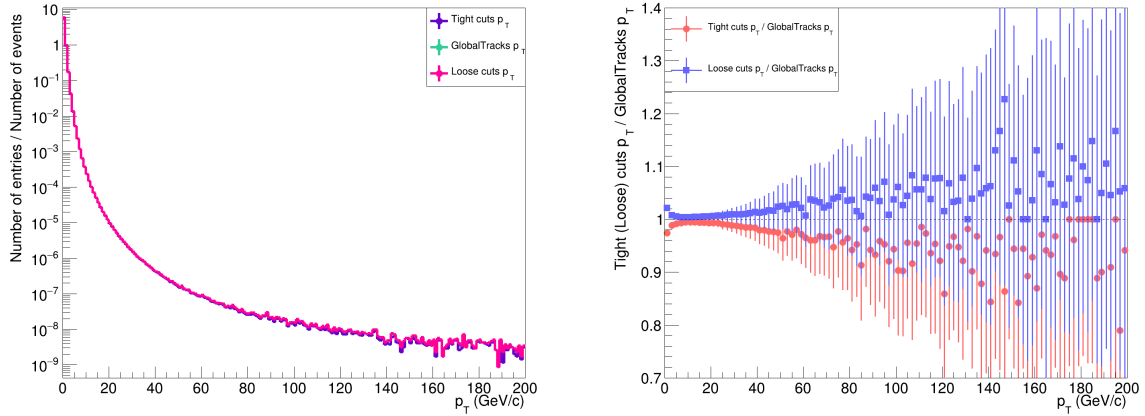
Figure 40: Left: comparison of the p_T spectra for GlobalTracks selection, tight cuts, and loose cuts. Right: ratios between tight cuts p_T spectrum over the GlobalTracks p_T spectrum (red) and between loose cuts p_T spectrum over the GlobalTracks p_T spectrum (blue).
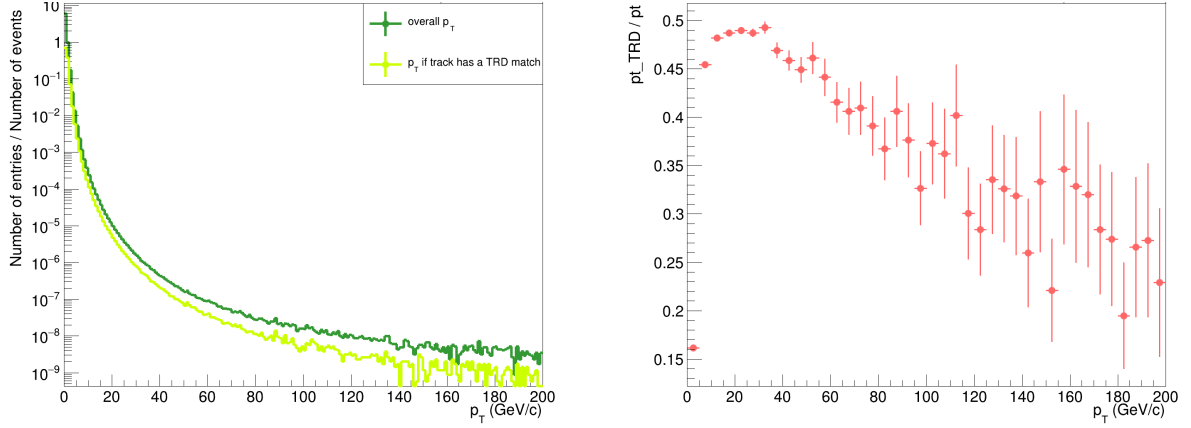
Figure 41: Left: comparison between the comprehensive $_T$ spectrum against the p_T spectrum for track with TRD match. Right: ratio of the p_T spectrum when tracks have TRD match over the overall p_T spectrum.
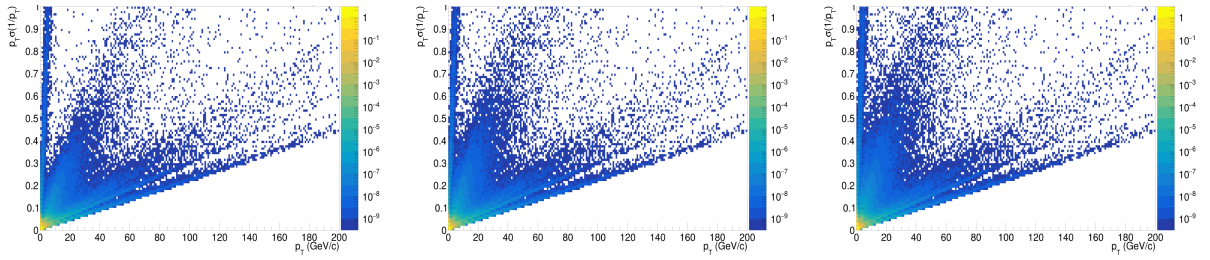
(a) Resolution of the transverse momentum when requiring hits in the 1st and 2nd ITS layers.
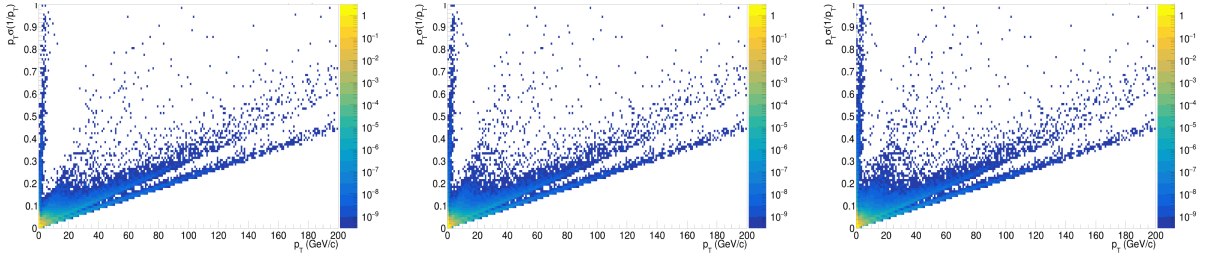
(b) Resolution of the transverse momentum when requiring hits in the 4th, 5th and 6th ITS layers.
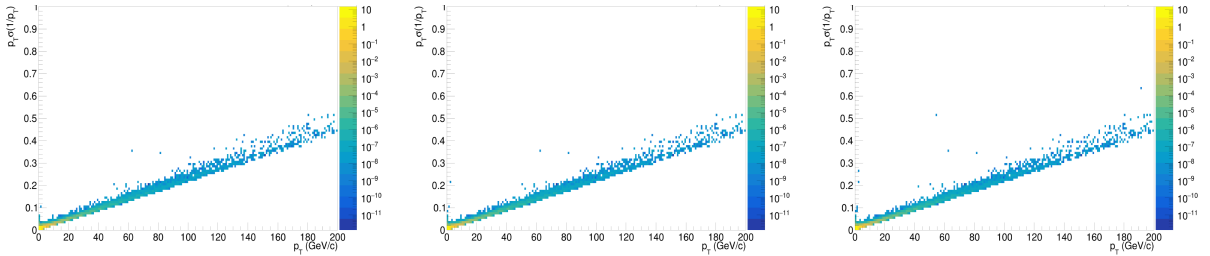
(c) Resolution of the transverse momentum when requiring tracks with TRD match.

Figure 42: Resolution of the transverse momentum for tight cuts, Global Tracks and loose cuts from left to right.
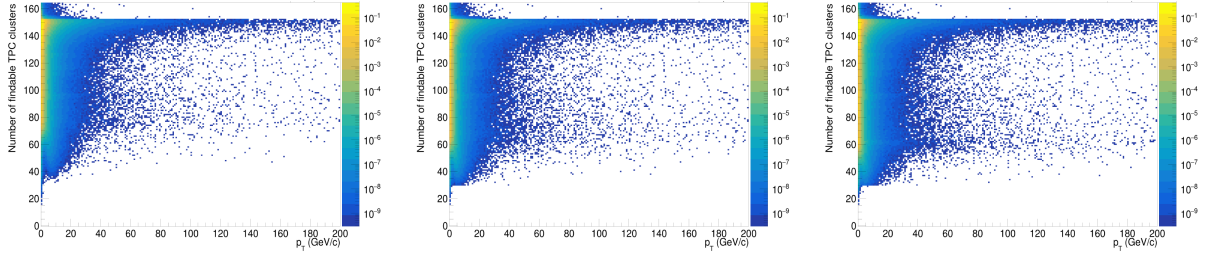
(a) Number of findable TPC clusters.
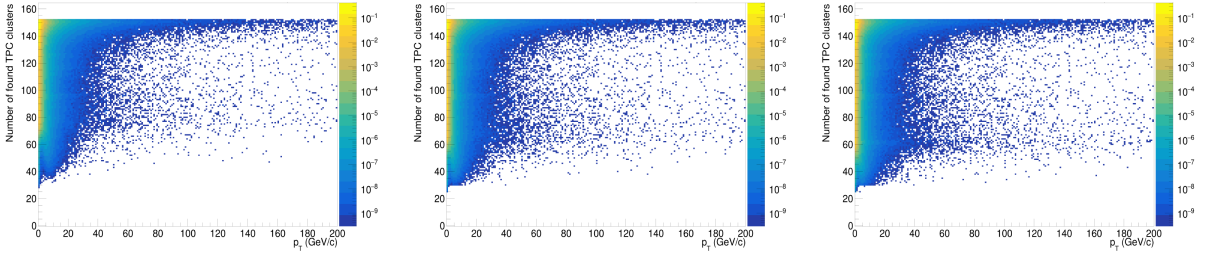
(b) Number of found TPC clusters.

Figure 43: Number of findable and found TPC clusters for tight cuts, Global Tracks and loose cuts from left to right.
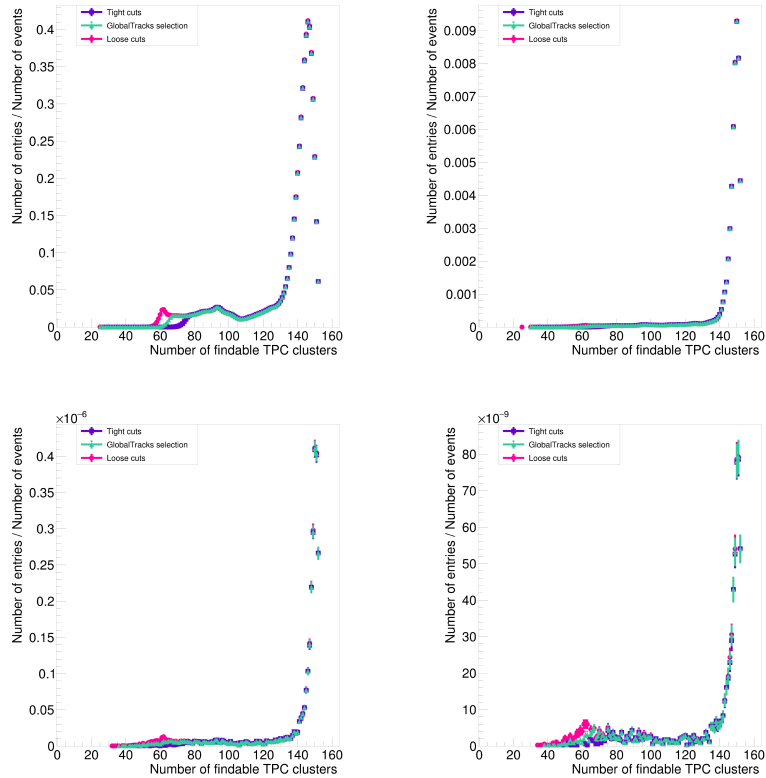
Figure 44: Projections of the number of found TPC clusters over the normalized number of events for four p_T ranges: $0 < p_T < 1$ GeV/c, $3 < p_T < 5$ GeV/c, $50 < p_T < 100$ GeV/c, $100 < p_T < 200$ GeV/c.
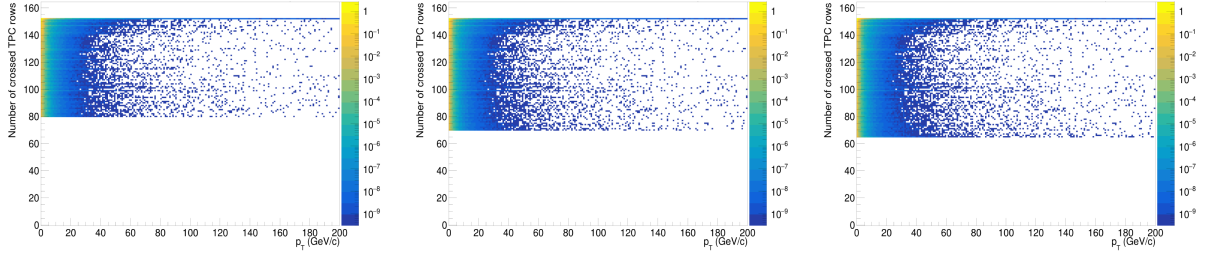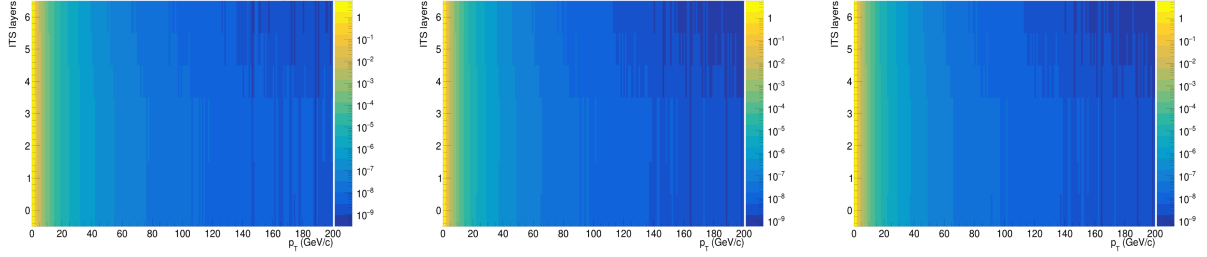
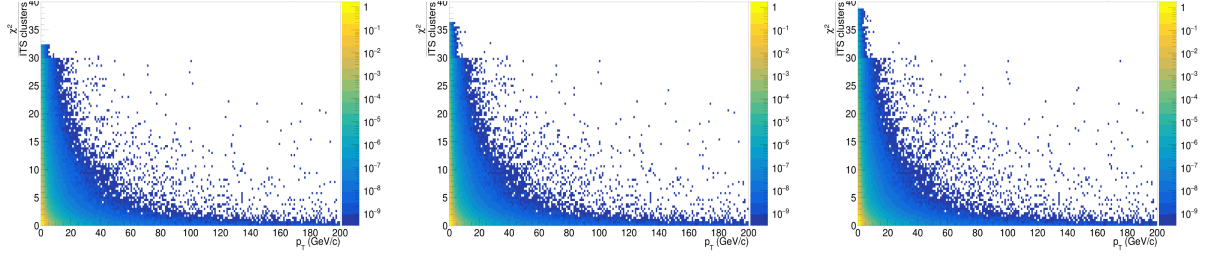(a) Number of crossed TPC rows for tight cuts, Global Tracks and loose cuts from left to right.
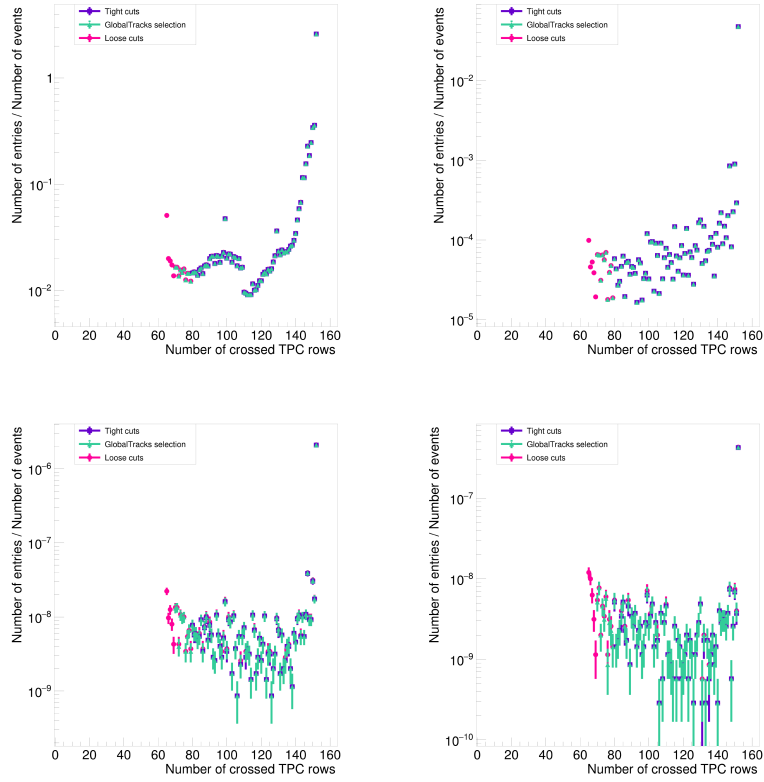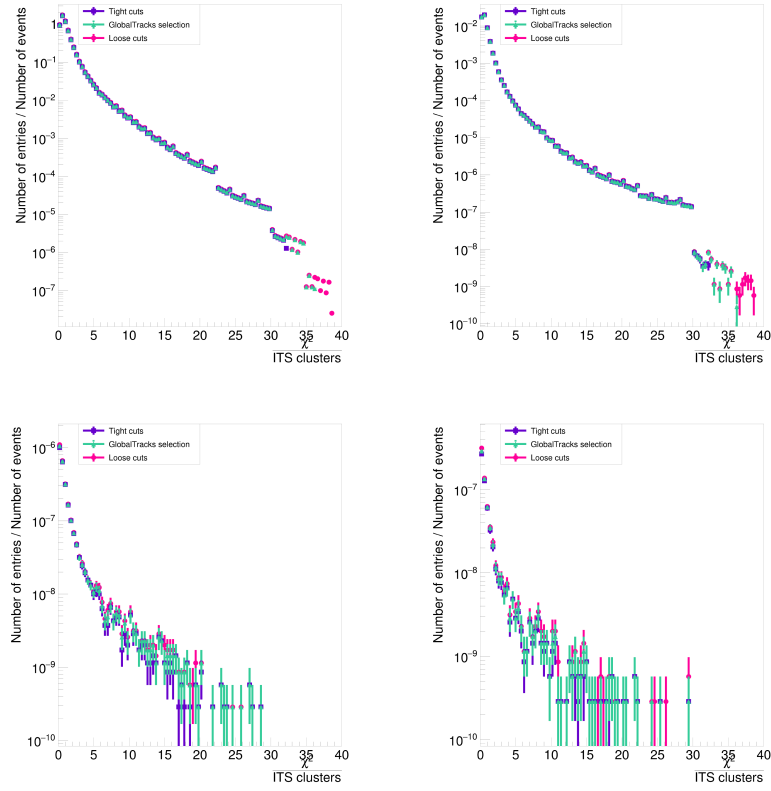

(b) Projections of the number of crossed TPC rows for four p_T ranges: $0 < p_T < 1$ GeV/c, $3 < p_T < 5$ GeV/c, $50 < p_T < 100$ GeV/c, $100 < p_T < 200$ GeV/c.

Figure 45
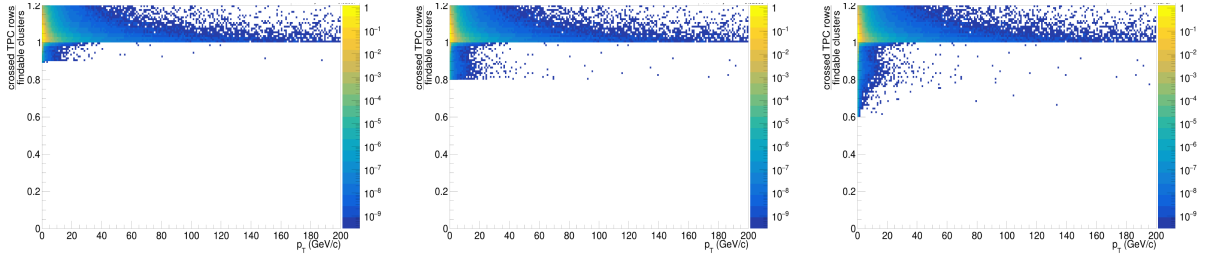
(a) Crossed TPC rows over findable clusters for tight cuts, Global Tracks and loose cuts from left to right.
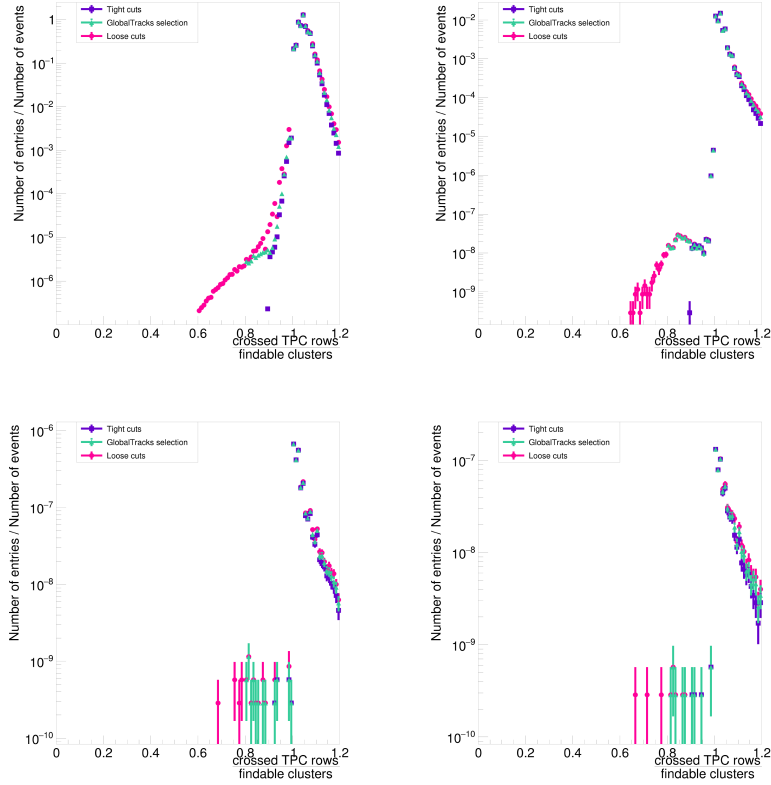
(b) Projections of crossed TPC rows over findable clusters for four p_T ranges: $0 < p_T < 1$ GeV/c, $3 < p_T < 5$ GeV/c, $50 < p_T < 100$ GeV/c, $100 < p_T < 200$ GeV/c.

Figure 46
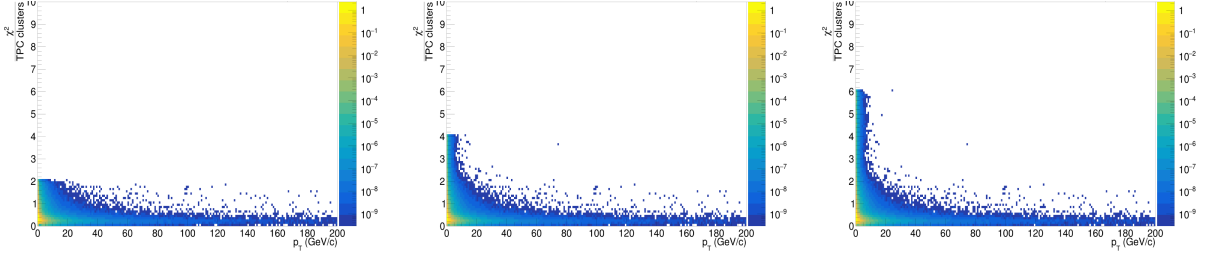
(a) χ^2 per TPC cluster for tight cuts, Global Tracks and loose cuts from left to right.
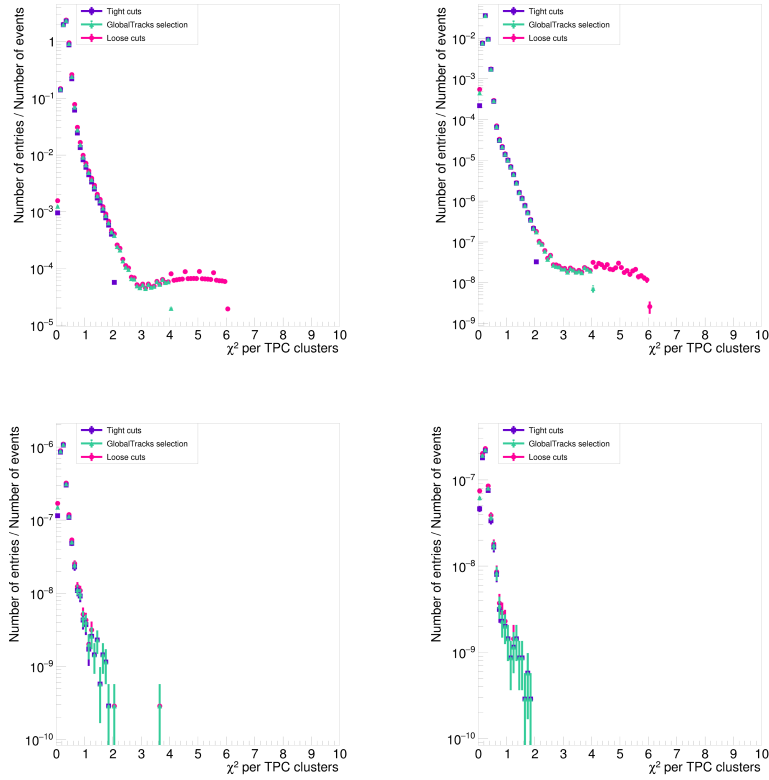

(b) Projections of χ^2 per TPC cluster for four p_T ranges: $0 < p_T < 1$ GeV/c, $3 < p_T < 5$ GeV/c, $50 < p_T < 100$ GeV/c, $100 < p_T < 200$ GeV/c.
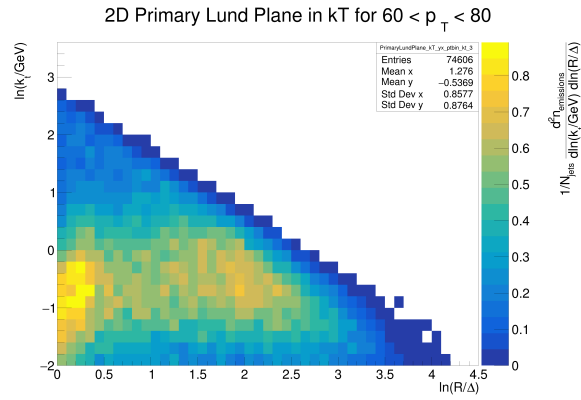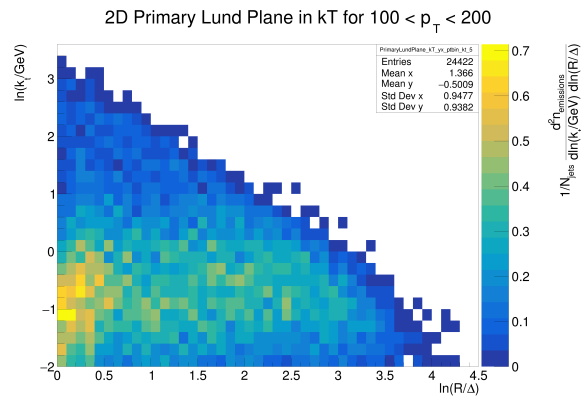
Figure 47
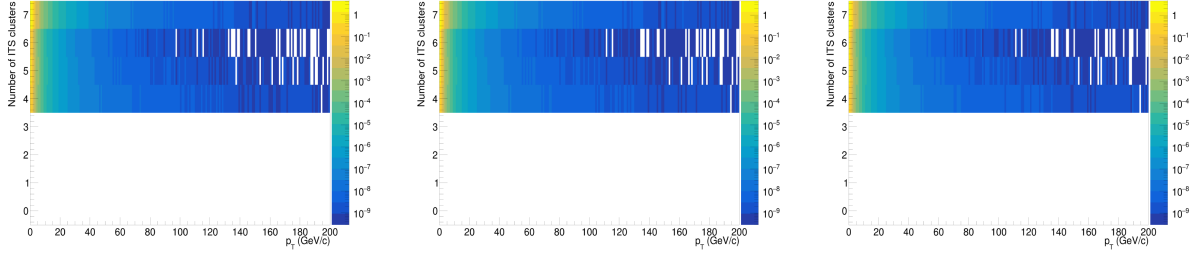
(a) Number of ITS clusters for tight cuts, Global Tracks and loose cuts from left to right.
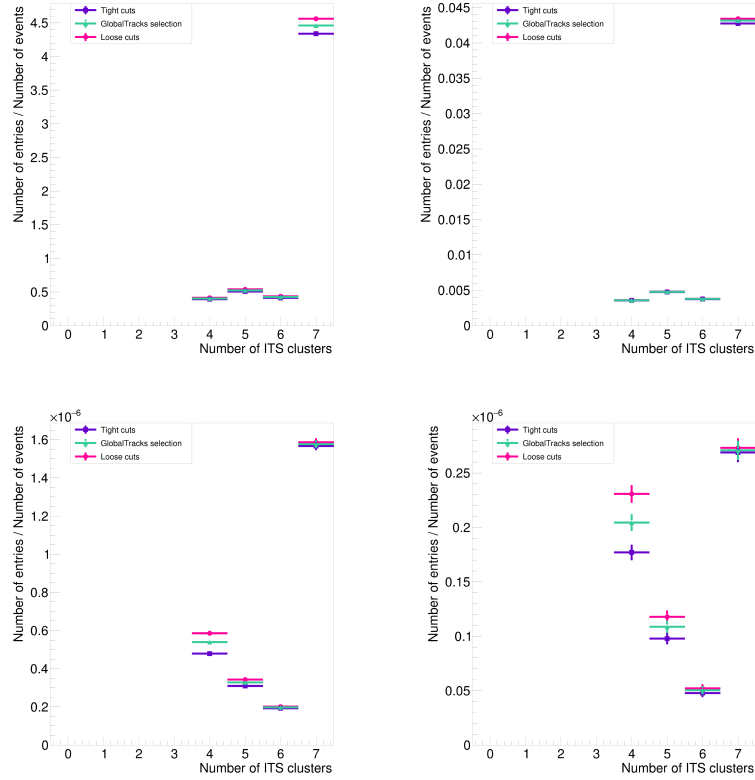
(b) Projections of the number of ITS clusters for four p_T ranges: $0 < p_T < 1$ GeV/c, $3 < p_T < 5$ GeV/c, $50 < p_T < 100$ GeV/c, $100 < p_T < 200$ GeV/c.

Figure 48

(a) ITS hitmap for tight cuts, Global Tracks and loose cuts from left to right.
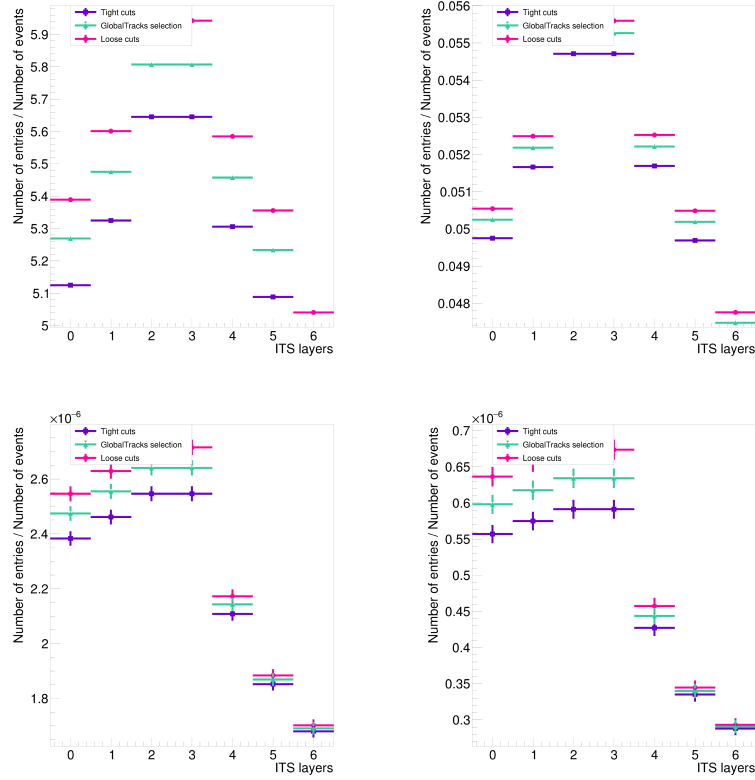
(b) Projections of the number of ITS layers for four p_T ranges: $0 < p_T < 1$ GeV/c, $3 < p_T < 5$ GeV/c, $50 < p_T < 100$ GeV/c, $100 < p_T < 200$ GeV/c.

Figure 49

(a) χ^2 per ITS cluster for tight cuts, Global Tracks and loose cuts from left to right.

(b) Projections of χ^2 per ITS cluster for four p_T ranges: $0 < p_T < 1$ GeV/c, $3 < p_T < 5$ GeV/c, $50 < p_T < 100$ GeV/c, $100 < p_T < 200$ GeV/c.

Figure 50

B   Appendix

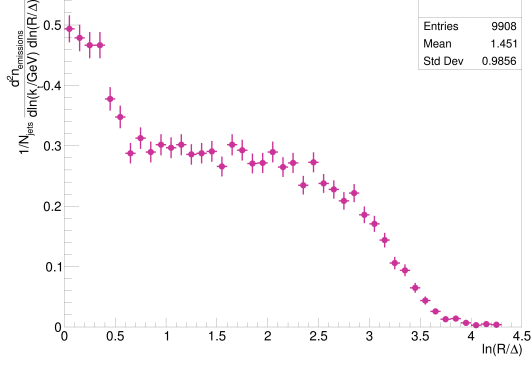This Appendix shows the Primary Lund plane results obtained from the `LHC22_pass4_lowIR` dataset.
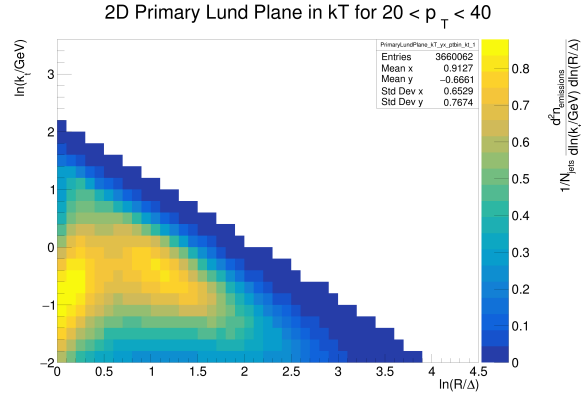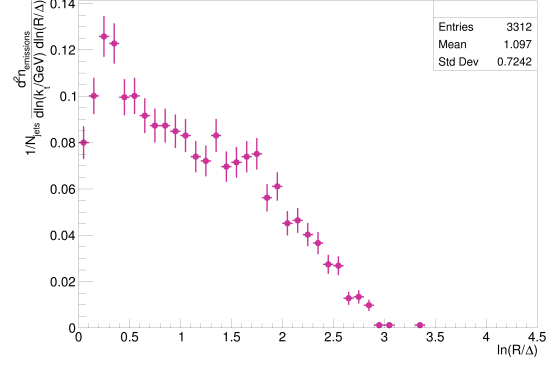

(a)

(b)

(c)

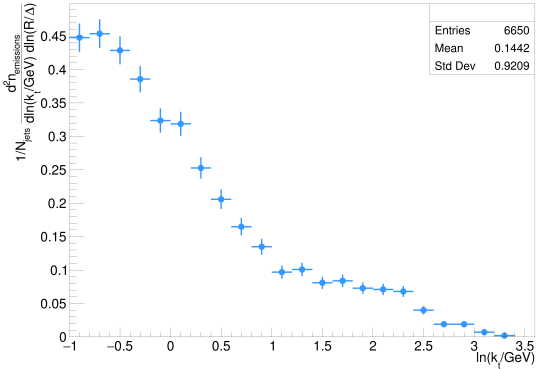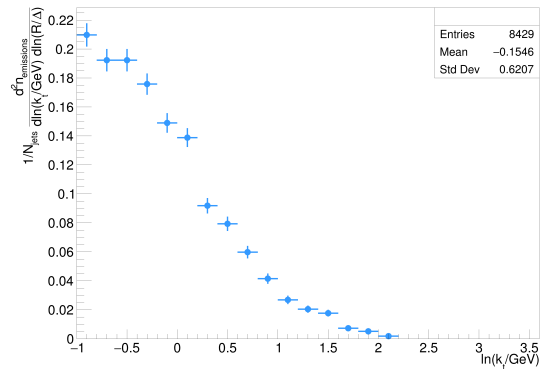Figure 51: Primary Lund plane in the (Δ, k_T) plane for different momentum ranges.

(a) Projection of the primary Lund plane density in the $100 < p_T < 200$ GeV/c range over the $\ln(R/\Delta)$ axis in the non-perturbative region ($-2 < \ln(k_T/\text{GeV}) < 0$).

(b) Projection of the primary Lund plane density in the $100 < p_T < 200$ GeV/c range over the $\ln(R/\Delta)$ axis in the perturbative region ($0 < \ln(k_T/\text{GeV}) < 3.5$).
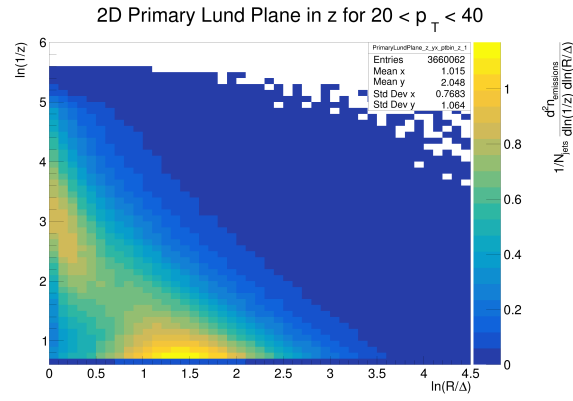
(c) Projection of the primary Lund plane density in the $100 < p_T < 200$ GeV/c range over the $\ln(k_T/\text{GeV})$ axis in the wide splitting region ($0 < \ln(R/\Delta) < 1$).
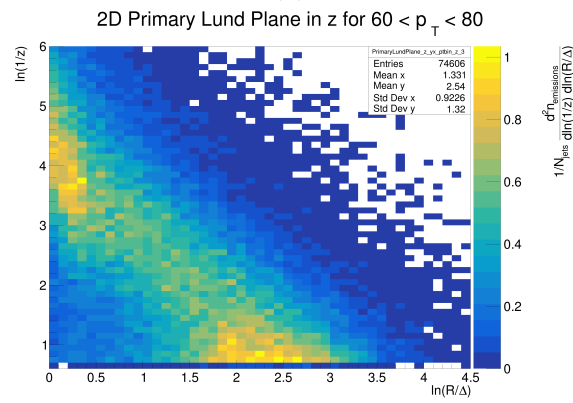
(d) Projection of the primary Lund plane density in the $100 < p_T < 200$ GeV/c range over the $\ln(k_T/\text{GeV})$ axis in the narrow splitting region ($1 < \ln(R/\Delta) < 4.5$).
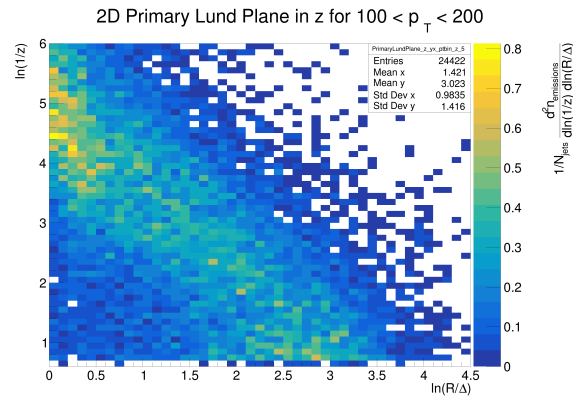
Figure 52: Slices of the Primary Lund plane density in the (Δ, k_T) plane.
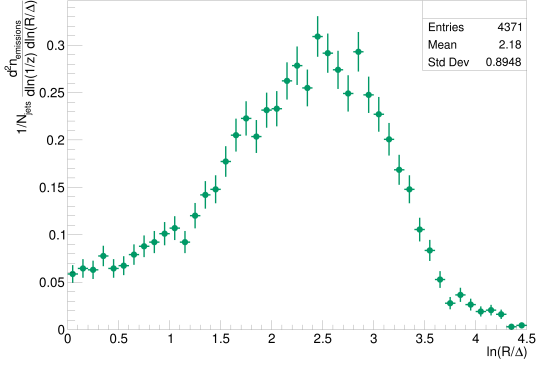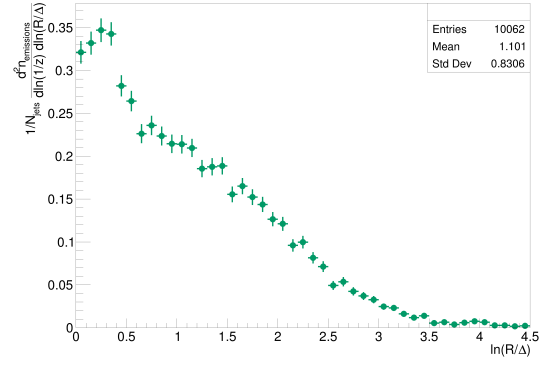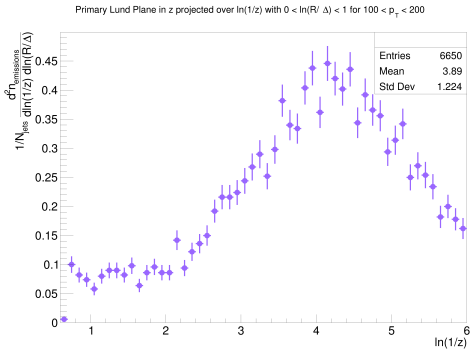
(a)

(b)

(c)

Figure 53: Primary Lund plane in the (Δ, z) plane for different momentum ranges.

(a) Projection of the primary Lund plane density in the $100 < p_T < 200$ GeV/c range over the $\ln(R/\Delta)$ axis in the non-perturbative region $(0.6 < \ln(1/z) < 2)$.
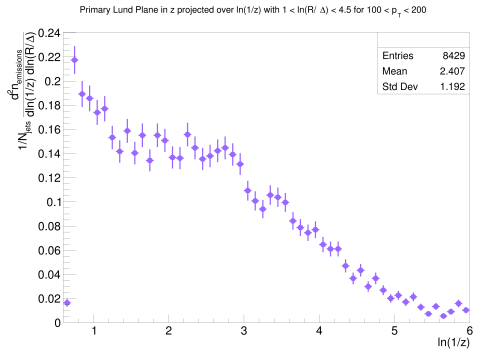
(b) Projection of the primary Lund plane density in the $100 < p_T < 200$ GeV/c range over the $\ln(R/\Delta)$ axis in the perturbative region $(2 < \ln(1/z) < 6)$.

(c) Projection of the primary Lund plane density in the $100 < p_T < 200$ GeV/c range over the $\ln(1/z)$ axis in the wide splitting region $(0 < \ln(R/\Delta) < 1)$.

(d) Projection of the primary Lund plane density in the $100 < p_T < 200$ GeV/c range over the $\ln(1/z)$ axis in the narrow splitting region $(1 < \ln(R/\Delta) < 4.5)$.

Figure 54: Slices of the Primary Lund plane density in the (Δ, z) plane.

Bibliography

[1] Robert Oerter. *The theory of almost everything: The Standard Model, the unsung triumph of modern physics.* Penguin, 2006.

[2] Cush. Standard model of elementary particles, 2019. `https://commons.wikimedia.org/wiki/File:Standard_Model_of_Elementary_Particles.svg`.

[3] Frank Wilczek. QCD made simple. *Phys. Today*, 53(8):22–28, 2000.

[4] Marta Verweij et al. *Modelling and measurement of jet quenching in relativistic heavy-ion collisions at the LHC.* Utrecht University, 2013.

[5] ALICE collaboration et al. The ALICE experiment-a journey through qcd. *arXiv preprint arXiv:2211.04384*, 2022.

[6] Boris L Ioffe, Viktor Sergeevich Fadin, and Lev Nikolaevich Lipatov. *Quantum chromodynamics: Perturbative and nonperturbative aspects.* Number 30. Cambridge University Press, 2010.

[7] Siegfried Bethke. Experimental tests of asymptotic freedom. *Progress in particle and Nuclear Physics*, 58(2):351–386, 2007.

[8] A Pandav, D Mallick, and B Mohanty. Search for the qcd critical point in high energy nuclear collisions. *Progress in Particle and Nuclear Physics*, 125:103960, 2022.

[9] Krishna Rajagopal, Gregory W Ridgway, Ryan Weller, and Yi Yin. Understanding the out-of-equilibrium dynamics near a critical point in the qcd phase diagram. *Physical Review D*, 102(9):094025, 2020.

[10] MA Stephanov. QCD phase diagram: An overview. *arXiv preprint hep-lat/0701002*, 2006.

[11] Eric M Metodiev. The fractal lives of jets, apr 2020. `https://www.ericmetodiev.com/post/jetformation`.

[12] José Guilherme Milhano. Theoretical overview of jet quenching. *arXiv preprint arXiv:1211.2657*, 2012.

[13] Frédéric A Dreyer, Gavin P Salam, and Grégory Soyez. The Lund jet plane. *Journal of High Energy Physics*, 2018(12):1–42, 2018.

[14] Bo Andersson, Gosta Gustafson, Leif Lönnblad, and Ulf Pettersson. Coherence effects in deep inelastic scattering. *Zeitschrift für Physik C Particles and Fields*, 43: 625–632, 1989.

[15] Andrew Lifson, Gavin P Salam, and Grégory Soyez. Calculating the primary Lund jet plane density. *Journal of High Energy Physics*, 2020(10):1–44, 2020.

[16] Georges Aad, Brad Abbott, Dale Charles Abbott, A Abed Abud, Kira Abeling, Deshan Kavishka Abhayasinghe, Syed Haider Abidi, OS AbouZeid, Nadine L Abraham, Halina Abramowicz, et al. Measurement of the lund jet plane using charged particles in 13 tev proton-proton collisions with the atlas detector. *Physical review letters*, 124(22):222002, 2020.

[17] ALICE Collaboration. Physics preliminary summary: Measurement of the primary lund plane density in pp collisions at.

[18] Kenneth Aamodt, A Abrahantes Quintana, R Achenbach, S Acounis, D Adamová, C Adler, M Aggarwal, F Agnese, G Aglieri Rinella, Z Ahammed, et al. The ALICE experiment at the CERN LHC. *Journal of Instrumentation*, 3(08):S08002, 2008.

[19] Media and CERN Press Relations (Press release). Large hadron collider restarts, 22 April 2022. `https://home.cern/news/news/accelerators/large-hadron-collider-restarts`.

[20] The large hadron collider, 2020. `https://home.cern/science/accelerators/large-hadron-collider`.

[21] Pcharito. Schematics of the ALICE subdetectors, 2014. `https://commons.wikimedia.org/w/index.php?curid=31365856`.

[22] Christine Nattrass, for the ALICE collaboration, et al. Measurements of jets in ALICE. In *Journal of Physics: Conference Series*, volume 589, page 012015. IOP Publishing, 2015.

[23] Matteo Cacciari, Gavin P Salam, and Gregory Soyez. The anti-kt jet clustering algorithm. *Journal of High Energy Physics*, 2008(04):063, 2008.

[24] CMS collaboration et al. A Cambridge-Aachen (CA) based jet algorithm for boosted top-jet tagging. Technical report, CMS-PAS-JME-09-001, 2009.

[25] Alice Caluisi. Jet Lund Declustering. `https://github.com/AliceO2Group/O2Physics/blob/master/PWGJE/Tasks/jetLundReclustering.cxx`, 2023.

[26] G. P. Salam M. Cacciari and G. Soyez. FastJet contrib. `https://fastjet.hepforge.org/contrib/`, 2014.

[27] ALICE LEGO train system. `https://alice-doc.github.io/alice-analysis-tutorial/analysis/lego.html#the-lego-train-system`.

[28] ALICE monitor system for LEGO trains. `http://alimonitor.cern.ch/map.jsp`.

[29] ALICE , et al. The alice transition radiation detector: Construction, operation, and performance. *Nuclear instruments & methods in physics research. Section A*, 881:88–127, 2018.

[30] Daan Leermakers. Systematic study of track quality cuts at alice. Technical report, 2015.

[31] Torbjörn Sjöstrand, Stephen Mrenna, and Peter Skands. A brief introduction to pythia 8.1. *Computer Physics Communications*, 178(11):852–867, 2008.

[32] Tanju Gleisberg, Stefan Höche, F Krauss, M Schönherr, S Schumann, F Siegert, and J Winter. Event generation with sherpa 1.1. *Journal of High Energy Physics*, 2009 (02):007, 2009.

[33] Johannes Bellm, Stefan Gieseke, David Grellscheid, Simon Plätzer, Michael Rauch, Christian Reuschle, Peter Richardson, Peter Schichtel, Michael H Seymour, Andrzej Siódmok, et al. Herwig 7.0/herwig++ 3.0 release note. *The European Physical Journal C*, 76:1–8, 2016.